Materials Horizons

ROYAL SOCIETY OF CHEMISTRY

REVIEW

View Article Online
View Journal | View Issue

Cite this: *Mater. Horiz.*, 2025, **12**, 8920

From solid to liquid piezoelectric materials

Minakshi Gill,[a] Marcell Tibor Máthé,[b] Péter Salamon,[b] James T. Gleeson [a] and Antal Jákli *[ac]

The history and evolution of piezoelectricity are reviewed, starting from the discovery of pressure (''piezo'' in Greek) electricity by the Curie brothers in a ferroelectric crystal until today, when liquid piezoelectricity is being observed in polar anisotropic fluids, namely, the ferroelectric nematic liquid crystal (N_F) materials. As effects analogous to the piezoelectricity have been observed in various crystals, polymers and biomaterials with lack of inversion symmetry, the definition of piezoelectricity has evolved to describe a linear coupling between mechanical stress and electric polarization. Mechanical stress-induced electric polarization is called direct piezoelectricity, and electric field-induced mechanical stress is called converse piezoelectricity. Soon after the discovery of ferroelectricity in chiral liquid crystals with two- and one-dimensional fluid order, owing to the lack of their inversion symmetry, linear electromechanical effects analogous to direct and converse piezoelectricity have also been observed in those materials. While these materials in certain directions can sustain static stress, the N_F phase is truly a three-dimensional fluid, and a steady stress can only be sustained by surface tension. The review concludes with a summary and analysis of direct and converse piezoelectric measurements on several N_F materials, followed by the challenges and possible future applications of liquid piezoelectricity.

Received 14th May 2025,
Accepted 22nd July 2025

DOI: 10.1039/d5mh00917k

rsc.li/materials-horizons

Wider impact

A mechanical stress-induced electric polarization is called direct piezoelectricity, and an electric field-induced mechanical stress is called converse piezoelectricity. The history of piezoelectricity (pressure electricity) started over 130 years ago by the discovery of the Curie brothers in a ferroelectric crystal, Rochelle salt. As effects analogous to the piezoelectricity have been observed in various crystals, polymers and biomaterials lacking inversion symmetry, the definition of the piezoelectricity has evolved to describe a linear coupling between mechanical stress and electric polarization. Soon after the discovery of ferroelectricity in chiral liquid crystals with two- and one-dimensional fluid order, owing to the lack of their inversion symmetry, linear electromechanical effects analogous to direct and converse piezoelectricity have also been observed in these materials that can still sustain static stress in certain directions. On the other hand, the newest liquid crystal phase, the ferroelectric nematic liquid crystal (N_F) phase is a truly three-dimensional fluid, and a steady stress can only be sustained by surface tension. It is therefore of principal interest to study and compare piezoelectricity of liquid N_F materials with solid and partially solid piezoelectric materials. In this review, we also discuss the challenges and possible future applications of liquid piezoelectricity.

I. Introduction

In 1880, Pierre and Jacques Curie[1] detected electric charges on some crystals (sodium chlorate, boracite, tourmaline, quartz, calamine, topaz, tartaric acid, sugar and Rochelle salt) when compressed in certain directions. The charge observed was found to be proportional to the pressure, and it disappeared when the pressure was removed. These observations mark the birth of ''piezoelectricity''; ''piezo'' is the Greek word for ''pressure''. Only one year later, Lippmann proposed[2,3] that the converse effect (*i.e.*, strain induced by electric charges) must also exist, owing to thermodynamics. This prediction was also verified by the Curie brothers.[4] The early history of piezoelectricity[5] was complete with Voigt's first rigorous formulation of piezoelectricity[6] in 1894.

The next stage is the birth of ultrasonic technology during the Great War in 1918. It was Langevin who applied both the converse and direct piezoelectric effects to both emit and detect sound waves underwater utilizing large plates of quartz.[7,8] Soon thereafter, Cady demonstrated that the frequency can be stabilized if a quartz crystal is used in resonance with an electrical oscillator.[9] Such quartz crystal oscillators were first used by the US National Bureau of Standards as frequency standards and

[a] *Department of Physics, Kent State University, Kent, Ohio 44242, USA. E-mail: ajakli@kent.edu*
[b] *Institute for Solid State Physics and Optics, Wigner Research Centre for Physics, P.O. Box 49, Budapest H-1525, Hungary*
[c] *Materials Sciences Graduate Program and Advanced Materials and Liquid Crystal Institute, Kent State University, Kent, Ohio 44242, USA*

later became critical in the development of broadcasting radio waves.[10]

The third wave of piezoelectricity studies began in the 1940s with the observation of new strong piezoelectric materials, especially barium titanate.[11–13] The field developed quickly with the subsequent discovery of piezoelectricity in certain polymers, both synthetic and biological, beginning in the 1970s.[14–19] The native effects in polymers and biomaterials[16] are generally small but can be increased by poling by strong DC electric fields, typically at elevated temperatures. Owing to their flexibility and ease of fabrication, piezoelectric polymers opened up a whole new vista of applications and/or device concepts that would not have been possible using conventional crystalline piezoelectrics. One particularly well-known and commercially attractive example is poly(vinylidene fluoride) (PVDF);[20] PVDF has been used in diverse applications ranging from infrared detector technology to audio speakers. More recently, certain cellular polymers (ferro-electrets) have also been found to behave like soft, sensitive piezoelectrics.[21–24] Fiber mats constructed of polylactic acid (PLA) dispersed with ferroelectric barium titanate (BT) nanoparticles were also found to be highly piezoelectric, having a 100× larger piezoelectric response per weight than that of single-crystal BT and pure piezoelectric ceramic fibers.[25,26] At present, solid piezoelectric materials are used in energy harvesting devices,[27] various sensors[28] and even in transistors (piezotronics).[29]

The mathematical description of piezoelectricity was originally developed for crystals subject to reversible compression and extension. This was later generalized to arbitrary strain/stress, including shear. Both stress $\hat{T}$ and strain $\hat{S}$ are represented by tensors of second rank. T_{ij} describes the ith component of a reversible force per unit area (*i.e.*, stress) acting in a surface element pointing in direction j. Tensor formulation is necessary when considering materials that are not isotropic. In this case, it is possible (for example) that applying force in one direction can lead to displacement in a different direction. Tensor formulation is the precise and compact methodology to account for all possible combinations of material response to external forces. An individual component of reversible strain is given by $S_{ij} = (\partial s_i)/(\partial x_j)$, where s_i is ith component of the displacement of a volume element from the equilibrium position. When we consider the case of a substance having equilibrium position subject to reversible displacement, we infer that the material displaces elastically, which is the case for crystals, ceramics and solid polymers when subject to sufficiently small stress/strain. With this in mind, the piezoelectric effects are illustrated in Fig. 1.

The direct piezoelectric effect when a macroscopic electric polarization vector $\vec{P}$ is produced by mechanical stress $\hat{T}$, can be expressed by the following equation:

$$P_i = \sum_{jk} \gamma_{ijk} T_{jk}, \quad (1)$$

where the coefficients of the third-rank tensor γ_{ijk} are known as the piezoelectric charge coefficients.

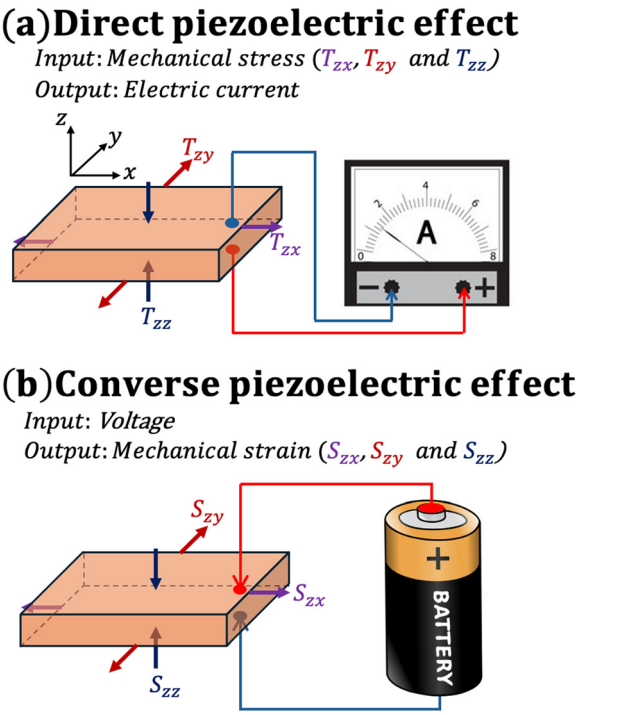

Fig. 1 Illustration of the direct (a) and converse (b) piezoelectric effects. Note: in (a), the output 'current' will only be induced when the stress is changing. For constant stress, it will be an induction of charge.

In the converse (or "inverse") effect, the material becomes strained when an external electric field $\vec{E}$ is applied. This is expressed as follows:

$$S_{jk} = \sum_i \gamma_{ijk} E_i, \quad (2)$$

where S_{jk} is the jk component of the strain tensor.

As pointed out by Lippmann,[3] both the direct and converse effects are manifestations of the same fundamental property of the substance: a linear coupling between a second-rank tensor (like strain or stress) and a first-rank tensor (such as the polarization or electric field vector). This is emphasized by the fact that the same coefficients γ_{ijk} are found in both the above-mentioned equations.

Of critical importance are the symmetries of the material in question. Hence, most substances do not exhibit piezoelectricity. Underlying this entire phenomenon is the Curie principle, which states that the tensor coefficients characterizing material properties should be invariant under the symmetry transformations of the substance.[30] Therefore, any material that possesses inversion symmetry transformations, *i.e.*, unchanged by the transformation $(x, y, z) \rightarrow (-x, -y, -z)$, would require that $\gamma_{ijk} = (-1)^3\gamma_{ijk}$, which can only be true if $\gamma_{ijk} \equiv 0$. This means that materials with inversion symmetry cannot be piezoelectric. In other words, piezoelectricity is only observable in materials that lack inversion symmetry. Furthermore, it is possible to identify which components of γ_{ijk} must vanish based solely on the symmetry group of any given material. As was pointed out by Woldemar Voigt[6] in 1894, 20 out of the 32 crystallographic

groups and 3 of the continuous point groups[31] lack inversion symmetry and so may exhibit piezoelectricity. The least symmetric materials with C_1 symmetry allow all γ_{ijk} to be non-zero. Since $\gamma_{ijk} = \gamma_{ikj}$, there can be at most 3 × 6 = 18 independent tensor elements.

Due to the technological importance of piezoelectric materials for transducers, frequency standards, ultrasonics, *etc.*, the third-rank tensor representation of the piezoelectric coupling constant is often replaced (for simplicity) by a 2nd-rank tensor following the convention below. Directions are identified using the three axes, labeled 1, 2 and 3, where 3 is chosen parallel to the direction of polarization. Since the 2nd-rank stress and strain tensors are symmetric, they have 6 independent elements and can be expressed as 6 × 1 tensors (6 element vectors): T_λ and S_λ, where $\lambda = \frac{(i+j)}{2}\delta_{ij} + [9-(i+j)](1-\delta_{ij})$, *i.e.*, 11 → 1; 22 → 2; 33 → 3; 23 = 32 → 4; 13 = 31 → 5; 12 = 21 → 6 transformations are used.[32] In this case, the piezoelectric charge constants are formally expressed as 3 × 6 element 2nd-rank tensors and denoted as d_{ij}. These are defined, along with several other piezoelectric constants and their definitions, in Table 1. These piezoelectric constants are various partial derivatives with respect to one independent parameter evaluated while another is held constant, as is typical in formulations of thermodynamics. These conditions can be regarded as ''mechanically free,'' ''short circuit,'' ''open circuit,'' and ''mechanically clamped,'' respectively.[33]

While these notations are simpler, they are also less transparent than the third-rank tensor notation. For this reason, where possible, in this study, we will retain the third-rank tensor formulation.

There is another coupling constant called the electromechanical coupling coefficient k, which is defined as the ratio of the mechanical energy accumulated in response to an electrical input or *vice versa*. It also corresponds to the fraction of electrical energy that can be converted into mechanical energy and *vice versa*.

Everything discussed above is related to solid piezoelectric materials. However, is this strictly restricted to solid materials, or can this phenomenon occur in fluids? Can liquids be piezoelectric? Isotropic liquids such as water, methanol, and acetone have an inversion symmetry, so piezoelectricity is forbidden. Recently, a ''fluid piezoelectric'' effect has been reported for an ionic liquid,[34] whereby upon compression, an electric signal proportional to the compression was observed. By definition it cannot be considered piezoelectric, since that fluid is isotropic with centrosymmetry, while genuine piezoelectricity requires the lack of inversion symmetry. In fact, it was subsequently determined that the effect is due to a reversible pressure-induced liquid-to-crystalline solid transition.[35] Such an effect results in an effective $d_{33} < 0.5$ pC N^{-1} piezoelectric coupling constant.

There are states of matter intermediate between crystalline solids and isotropic liquids. These are liquid crystals that possess less than three-dimensional solid behavior. ''Nematic (N)'' liquid crystals are three-dimensional liquids but anisotropic, *i.e.*, have long-range orientational and short-range positional order. ''Smectic (Sm)'' liquid crystals have a layered structure with one-dimensional positional order. Accordingly, they are one-dimensional solids and two-dimensional liquids. Finally, ''columnar (Col)'' liquid crystals have a two-dimensional positional order, so they are two-dimensional solids and one-dimensional liquids. Along their liquid directions, where there is no positional order, liquid crystals are also unable to support shear stress.[36] However, they also have some degree of density periodicity in the smectic and columnar phases, so they have the ability to sustain some elastic strain along their positional order (solid direction).

Significantly, several categories of liquid crystal materials lack inversion symmetry; therefore, they allow the existence of non-zero, piezoelectric-type third-rank tensors. The origin of this symmetry property may arise, *e.g.*, because of molecular chirality and/or polar molecular packing, as studied extensively[37–49] and will be discussed in Section 3 for chiral nematic (N*), ferroelectric tilted smectic (SmC*)[50,51] of chiral rod-shaped molecules, tilted columnar[52] phase of chiral disc-shaped molecules, and tilted polar smectic (SmCP)[53] phases of bent-core liquid crystal phases. Their symmetry allow the existence of piezoelectric charge coupling constant that may involve stress either along their solid or liquid directions. The question is whether we can call a linear coupling between electrical and mechanical fields as piezoelectric if they involve fluid direction or should we just talk about linear electromechanical effects. Certainly nothing is wrong to talk only about linear electromechanical effects as piezoelectricity belongs to that category as well. However, it is also possible to generalize the definition of the piezoelectricity to liquids if their symmetry allows it. The advantage of this approach is that it would group together phenomena in materials with the same underlying symmetry. In this review, we are following this approach: generalize strain for liquid directions and compare the same symmetry-enabled linear electromechanical effects among solid and fluid materials.

The definition of strain tensor $\hat{S} = \vec{\nabla} \cdot \vec{s}$ to be valid in liquids can be done only for periodic motions, where the displacement vector is $\vec{s}(t) = \vec{s}_o \cdot e^{i\omega t}$, where ω is the angular frequency of the vibration. For static cases, the displacement and the calculated piezoelectric coupling constant determined by this way would increase in time, and even for periodic situations, the piezoelectric constant could show abnormal frequency behavior due

Table 1 Various piezoelectric constants used in the literature with their definitions[33]

Symbol	Name	Definition
d	Piezoelectric charge coefficient or piezoelectric strain coefficient	$d_{ij} = \left(\frac{\partial D_i}{\partial T_j}\right)_E = \left(\frac{\partial S_j}{\partial E_i}\right)_T$
g	Piezoelectric voltage coefficient (voltage output constant)	$g_{ij} = -\left(\frac{\partial E_i}{\partial T_j}\right)_D = \left(\frac{\partial S_j}{\partial D_i}\right)_T$
e	Piezoelectric stress coefficient	$e_{ij} = -\left(\frac{\partial T_j}{\partial E_i}\right)_S = \left(\frac{\partial D_i}{\partial S_j}\right)_E$
h	Piezoelectric stiffness coefficient	$h_{ij} = -\left(\frac{\partial E_i}{\partial S_j}\right)_D - \left(\frac{\partial T_j}{\partial D_i}\right)_S$

to the viscous nature of the stress. The static displacement in liquids would be limited by the size of the fluid sample. Microscopic size liquid objects have elastic response due to the dominance of the surface tension, thus providing an additional argument for talking about piezoelectric effects in those fluids.

The justification for such treatment is provided by the recent discovery of ferroelectric nematic liquid crystals that are polar orientationally ordered three-dimensional fluids.[54–60] In spite of their genuine 3D fluidity, in electric fields they often behave as solid particles or microrobots,[61] they can also form metastable freestanding filaments[62,63] that can be stabilized in small electric fields.[63]

The main motivation of this paper is to review and compare the piezoelectric phenomena observed in a wide range of materials from crystalline solids to 3D liquids. We will overview the main properties of solid piezoelectric materials such as crystals, ceramics and polymers, and compare their behavior with polar nematic, smectic and columnar liquid crystals that can be regarded as three-, two-, and one-dimensional solids. Special emphasis will be devoted to recent measurements of converse[64] and direct[65] piezoelectric responses of ferroelectric nematic liquid crystals, for which we will present new results as well. Finally, this review concludes with a comprehensive analysis of the results followed by a future outlook.

II. Measurement techniques

II.A. Solid piezoelectric materials

Measuring piezoelectric effects in solid materials is well established.[66–68] Herein, we review some basics as well as important milestones. It is instructive to recall that at its most elemental state, piezoelectricity means an electrical response resulting from the application of pressure. In that regard, and its simplest form, one applies pressure to a material and detects an electrical change, be it the appearance of charge separation, an electric current or a potential difference. Of course, these are all related to one another. Thus, measuring piezoelectricity is, at least conceptually, rather simple: apply stress to a material and measure the resulting electrical signal (see Fig. 1a), as was done by the Curies. While conceptually simple, it is rather unspecific. One could easily face difficulties in reproducibility by using two different material specimens, perhaps having different shape or growth conditions, put them in the same apparatus and measure two different electrical responses.[69]

The much more specific measurement is not only the manifestation of ''piezoelectricity'', but the measurement of the piezoelectric coefficient(s), that is individual elements of the $\hat{\gamma}$ tensor in eqn (1). However, accompanying more specificity is a substantially more complicated measurement. This is more complex because such a measurement necessitates controlling the application of stress as well as the symmetry axes of the material to be studied. Implicit in this requirement is that the sample of material should have well-defined axes, *i.e.*, a single-crystal specimen.[70] Moreover, the individual axes need to be identifiable, either through prior crystallographic study of the specimen, or, in some cases, knowledge of the characteristic shapes formed by single crystal specimens. For example, quartz crystals frequently exhibit recognizable facets that accurately represent various symmetry axes. This knowledge and the ability to apply stress in a particular and known direction with respect to these axes allow the determination of individual elements of the piezoelectric charge tensor $\hat{\gamma}$, or alternatively the piezoelectric charge (or voltage) coefficient(s).

Very similar considerations apply when attempting to measure the inverse piezoelectric effect. That is, to apply an electrical potential difference and measure the resulting strain (see Fig. 1b). Similar to the case of direct piezoelectricity, if the goal is to measure the inverse piezoelectric ''response'', it is conceptually simple. How much strain results from an applied potential difference? If the goal is to examine inverse piezoelectric coefficients, the same issues apply, but in a different sense. For an inverse measurement, one must apply an electric field in a specific (and known) direction with respect to crystallographic axes. Then the resulting strain has to be determined compared to crystallographic axes. Measuring inverse piezoelectricity in crystalline materials, however, implies an additional complication in addition to the issues of orientation described above. Most crystalline materials have moduli exceeding 10 GPa, which means that the induced strains are in general rather small and not straightforward to measure directly. Different approaches to that problem are noted below.

II.A.1. Measurement examples. Perhaps the first choice one must make in measuring piezoelectricity concerns time dependence. With a few exceptions, the choice is usually between ac and dc. The Berlincourt technique[71] (see Fig. 2) is standard for measurements at low frequencies, below 10 kHz or so. This is sometimes termed ''quasistatic'' piezoelectricity.

True dc (*i.e.*, zero frequency) measurements are particularly difficult because of slow charge drift, finite electrical conductivity, *etc.* The quasistatic method is perhaps the simplest to

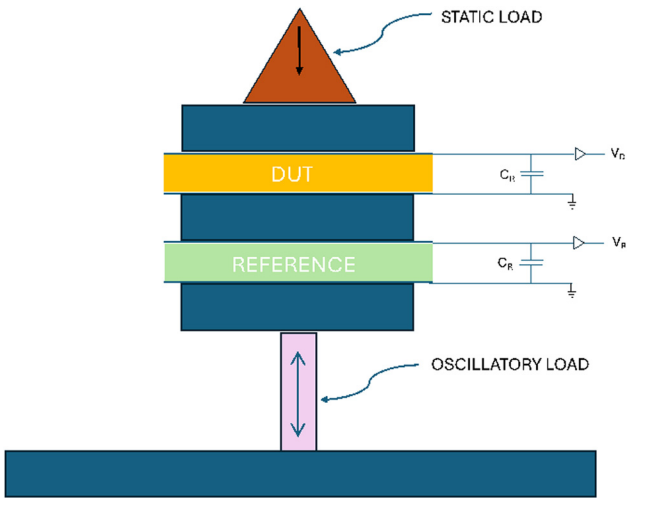

Fig. 2 Schematic of the Berlincourt technique.

implement, and there exists a handful of commercial instruments which are useful for determining d_{33}. This method has the advantage that it directly compares the piezoelectric response of an unknown material (''DUT'' in Fig. 2) to a reference material (usually lead zirconium titanate). Typically, one also employs a static force as a pre-load to prevent the motion of the apparatus. The oscillatory load is usually sinusoidal, so that sensitive, phase-locked measurement techniques can be used to measure the piezoelectric charge induced. However, studies have been performed, which question the reproducibility and accuracy of this method from material to material and laboratory to laboratory. It is perhaps most valuable for comparison between different materials or specimens that can be measured using one specific instrument and measurement protocol.

Techniques to determine multiple piezoelectric tensor coefficients at high frequency are better controlled, but unquestionably more difficult to implement. These techniques rely on the known resonant and anti-resonant frequencies of specifically shaped crystal samples as well as measurements over a wide frequency range. Such measurements, along with an ingenious formulation,[72] allow simultaneous measurement of four elements of the piezoelectric tensor and six components of the elastic tensor. The drawback is that it requires highly precise preparation of single crystal specimens that have been cut to exact shapes along specific crystalline axes. Such a technique is not ideal for high throughput analysis.

As noted above, the direct measurement of converse piezoelectricity in crystals is made difficult because the induced strain is small. Two approaches have been fruitful, however. *In situ* methods, in which an electric field is applied to a specimen that is housed within an atomic scattering device, such as an X-ray or neutron diffraction apparatus, do allow direct measurement of strain but only the strain within a small scattering volume of the apparatus.[73] A popular alternative is the laser interferometric method.[74] This technique allows measurement displacements in the nanometer range, which is sufficient to observe converse piezoelectricity. The drawback of both of these techniques is that they are neither simple nor inexpensive.

The above-mentioned methods are applicable when a single crystalline specimen is available. This is not always practical or even achievable. Two notable examples would be thin-film and powdered (or sintered) materials. In both of these, the challenge for measuring piezoelectricity is that the crystalline axis of the specimen is either unknown or highly randomized in space. In this case, even though stress may be applied, the relationship between the stress tensor and the crystalline axes is undetermined. In these situations, it is necessary to pole the piezoelectric before measurement. Poling involves subjecting the material to a sufficiently high electric field for an extended time. That is, a field strong enough to, for example, rotate microcrystalline particles (in a sinter) along the poling direction. In a polycrystalline sample, poling can enlarge grains having a dipole moment along the poling field at the expense of those in a competing direction. The poling field should exceed the coercive field. In this process, both time and temperature are important, and poling close to, but less than, the Curie temperature is more efficient.

II.B. Soft piezoelectric materials

Investigating the piezoelectric properties of soft materials and fluids is, conceptually at least, the same process as for solids. Specifically, to study direct piezoelectricity, one measures electrical signal(s) generated in response to mechanical excitation (strain or stress). In case of inverse piezoelectricity, we measured the mechanical response (deformation, vibration, or stress) induced by an electric field. From the point of view of basic understanding of the electromechanical phenomena observed in a specific soft or fluid material, it is important to determine the distinct components of the piezoelectric coupling tensor, which can be more challenging compared to crystalline solids, in that the axes of symmetry of the material may not be static because the materials are soft.

As in the case of solid crystals, the symmetry axes, crystallographic directions must be determined and appropriately configured with respect to the direction of deformation (for direct) or to the electric field (for converse). This is necessary to discern specific information about the given component of the piezoelectric coupling tensor in any material. For liquid crystals, a well-developed technique to achieve ''liquid single crystals'' is based on controlling the boundary conditions of the local average molecular direction (the ''director'') by surface orienting layers. Alternatively, the use of other external fields, *e.g.*, magnetic, is also possible.

In almost all liquid crystal display technologies, and very frequently diverse research endeavors as well, the liquid crystals are introduced between two parallel glass plates separated by a fixed distance that is usually much smaller than the plate size. This geometry is usually referred to as a ''sandwich cell''. Generally, the glass surfaces have been treated to control the boundary value(s) of the liquid crystal's optic axis (the director). In this manner, and under static conditions, the internal structure of the liquid crystal held between the plates becomes a boundary value problem to minimize the free energy density. There are two main types of surface alignments, respectively, known as homeotropic and planar. In homeotropic, the director boundary condition is perpendicular to the glass plates, and in planar, it is parallel and in a common direction. Usually both types are based on anisotropic interaction between the LC and a polymer thin layer. Different polymer coatings are used for homeotropic and planar alignments.[75]

To achieve planar orientation, the polymer chains are usually aligned by rubbing along the favorable direction. Commonly, planar alignment is considered to establish strong anchoring. In most cases, the director does not lie perfectly in the plane of the substrate at a planarly treated surface. It is tilted by a small angle (1°–5°) called pretilt in the plane that is perpendicular to the substrate and parallel with the rubbing direction. The pretilt is uniform and it depends on the materials used. Rubbing breaks the symmetry and provides a tool for polar alignment of the spontaneous polarization in ferroelectric

nematic liquid crystals, which are of special interest from the point of view of piezoelectricity.[64] In such polar materials, a uniform structure is achieved with parallel rubbing direction on the opposite boundaries, while antiparallel rubbing leads to a twisted structure. Besides rubbed polymers, obliquely evaporated SiO thin layers forming anisotropic periodic surface structures can also be used to achieve planar orienting layers. An emerging technique is the so-called photo-alignment[76,77] that uses light sensitive materials and linearly polarized light to align the molecules or polymer chains properly.

Homeotropic alignment can be achieved by coating of polymers that have amphiphilic parts preferring perpendicular orientation with respect to the substrate. Alternatively, silane-based monolayers are also often used to achieve homeotropic alignment, for example, dimethyloctadecyl[3-(trimethoxysilyl)-propyl]ammonium chloride (DMOAP) and octadecyltrichlorosilane (OTS). With the given boundary conditions, different types of liquid crystals will adopt different static configurations. Depending on the plate separation and the helical pitch, chiral phases may exhibit twisted structures instead of a uniform one.

In contrast to solid piezoelectric crystals, soft or fluidic materials are much easier to deform, therefore preserving the symmetry axes with respect to the deformation or the direction of the electric field may be much more difficult, even impossible. While surface alignment can be useful to maintain a liquid single-crystal structure effectively up to a few micrometers thickness, at larger sizes, liquid crystals tend to suffer from faults in the orientational field by forming defect structures and domains of different orientations separated by domain walls. Upon dynamic deformation, the material flow is induced in fluids, which can affect the structure and distort the original liquid single crystal. This phenomenon is called flow alignment, and it is due to the coupling between director rotation and material flow.[75] The reorientation of the spontaneous polarization by a strong electric field (poling) may be possible in soft or fluidic materials as well. Nevertheless, such poling may not have long-lasting effects because of the back relaxation of the spontaneous polarization into its original equilibrium state.

The measurement of direct piezoelectricity in fluids or soft materials requires the following components: mechanical actuator, deformation analyzer, sample holder, and electrical signal detector, as shown in Fig. 3. To investigate the inverse effect, the components are similar, but instead of a mechanical actuator and an electrical signal detector, a voltage source is needed, while the same deformation analyzer can be applied to determine the mechanical response of the material. In the following paragraphs, we overview the details of the apparatuses mentioned above.

The role of the mechanical actuator is to generate a linear periodic movement (vibration) that is used to create deformation in the studied material. The two basic parameters of the vibration are the amplitude A and frequency f. Mechanical actuators such as the Scotch yoke are used for low frequency ($f \lesssim 10$ Hz) and large amplitude ($A \gtrsim 1$ mm).[78] At intermediate frequencies (10 Hz $\lesssim f \lesssim$ 20 kHz), loudspeakers are commonly

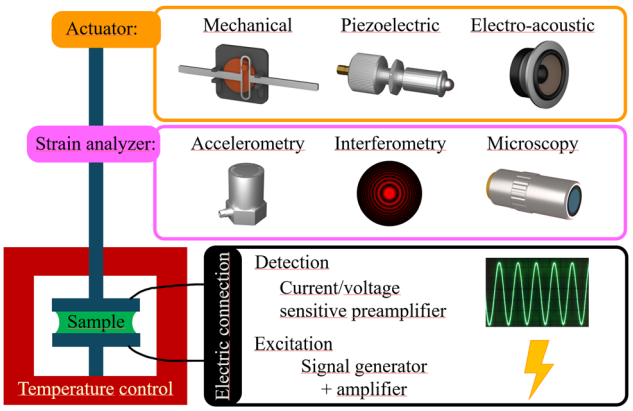

Fig. 3 Main components of electromechanical experiments for soft materials.

applied,[43] while at higher frequencies ($f \lesssim 100$ kHz) and small amplitudes, piezoelectric actuators are available.

The electrical response of the system can be characterized by measuring electrical current using a current sensitive preamplifier or by measuring the voltage drop on a relatively low, known resistance. Moreover, the response with the open circuit, or high impedance load can be characterized by measuring the induced voltage by the deformation.

To characterize both the direct and inverse piezoelectric effects, the deformation amplitude must be precisely determined. At higher amplitudes, a straightforward technique is optical microscopy. At lower amplitudes than the optical resolution, interferometric methods can be applied. Except at low frequencies, a convenient option is to use accelerometers combined with the lock-in technique, which allows an easy and precise evaluation of deformation amplitudes even as low as the nanometer range.[48]

III. Comparisons between piezoelectric materials

III.A. Three-dimensional solid piezoelectric materials

In contrast to naturally occurring materials such as quartz, or serendipitously discovered Rochelle salt, new piezoelectric materials with a perovskite structure, such as barium titanate (BT) and lead zirconate titanate (PZT), were prepared. These piezoelectric ceramics display significantly higher piezoelectric constants compared to the first piezoelectrics (see Table 2). However, to exhibit piezoelectric behavior, these materials must first undergo a process known as poling.[79] Due to their excellent piezoelectric properties, stability, and cost-effectiveness, ceramic materials have become the most widely used class of piezoelectric materials.[80]

Since its discovery in 1950, PZT has become one of the most widely used piezoelectric materials in technologies such as sensors or actuators.[81] However, it has a large Young's modulus that limits the extent to which it can deform.[82] Additionally, it contains the toxin lead, which makes it unsuitable for many applications because of health/environmental concerns.

Table 2 Properties of ceramic piezoelectric materials

	d_{33} (pC N^{-1})	g_{33} (V m N^{-1})	k	Y (GPa)	T_C (°C)	Advantages	Limitations
Lead zirconate titanate (PZT)	360	0.025	0.6–0.7	65	350	Stable, strong, degradation-resistant, high resonant frequency. Used in micro-sensors for energy harvesting and AFM	Rigid, high impedance, limited energy harvesting and applications. Lead content makes it unsuitable for body-implanted devices
Potassium sodium niobate (KNN)	Pure: 80–180,[93] modified: <700	0.047	0.51	104	400	High Curie temperature, lead-free, safe for medical implants and energy harvesting	KNN properties are inferior to PZT, and difficult processing limits its applications[94]
Barium titanate (BT)	Pure: 191, modified <620	0.011	0.49	67	130	High capacitance, used in sonar detection, phonograph needles, and actuators.	Low Curie temperature, poor temperature stability[95]
Bismuth sodium titanate (BNT)	Pure: 75, doped: 173	—	~0.21	93.3	<290 With dopant: >300	Lead-free, ideal for actuators due to high strain response	High electric field needed for large strain, the large strain hysteresis[86]
Aluminum nitride (AlN)	5	0.1	0.23	344.83	>2000	Used in MEMS, AlN thin films are ideal for resonators and sensors	Low piezoelectric coefficient, difficult fabrication[96,97]
Lithium niobate	6	0.023	0.23	202	1150	MEMS resonators	
ZnO nano generators	9.2, 12.4	0.13	—	40		Used in self-powered nano-devices and field-effect transistors	
Lead magnesium niobate-lead zirconate titanate (PMN–PZT) (S-crystal)	1530	0.036	0.93	65.9–99.6[98]	211	Actuators, ultrasonic transducers and transformers due to high dielectric permittivity and high piezoelectric coefficients[99]	
Lead magnesium niobate-lead titanate (PMN-30%PT (single crystal)	2000	0.040	0.93	~117[100]	137	Large displacement actuators, medical ultrasonic imaging transducers with superior broadband characteristics	Low Curie temperature, not good for flexible and wearable electronics due to rigidity and fragility
Sm–PMN–PT	4100	0.037	0.95	—	121	Good uniformity, room temperature applications, *e.g.*, for high-frequency medical imaging and low field-driven actuators	Low Curie temperature limits high temperature applications
Nd–PMN–PT	3090	0.028	0.95	—	138	Strong candidates for high-performance piezoelectric transducer	

Smolensky *et al.* discovered one of the most important lead-free piezoelectric materials, $Bi_{0.5}Na_{0.5}TiO_3$ (BNT), in 1960.[83] BNT has piezoelectric constant of 75 pC N^{-1} which can be enhanced to 173 pC N^{-1} by adding specific dopants.[84] These compounds exhibit exceptionally high strain, making them highly desirable for actuator applications.[85] However, as a high driving electric field is required to trigger a large strain and the large strain hysteresis,[86] it is difficult to use them in many applications. These challenges were resolved by introducing another environmentally friendly lead-free $K_{0.5}Na_{0.5}NbO_3$ (KNN) ceramic, where it provides a relatively high unipolar strain with reduced strain hysteresis in a low-strength driving electric field.[87] Undoped KNN has a piezoelectric constant between 80 and 160 pC N^{-1}, which can be increased up to 700 pC N^{-1} by fabricating the highly textured form of KNN-based ceramics.[88–91] In addition to its use in high-temperature applications, KNN is also valuable in energy harvesting and biomedical devices.[92]

Barium titanate (BT)-based ceramics are other promising high-strain piezo-materials, first discovered during World War II[11–13] It was the first perovskite-structured ferroelectric material and was widely used in sonar applications and phonograph needles.[101,102] As an alternative to PZT, BT has gained significance in actuator applications.[103] Aluminum nitride (AlN) and lithium niobate are lead-free piezoelectric ceramics with the advantage of a high Curie temperature exceeding 1000 °C,[104] although they have low piezoelectric constants of 5 pC N^{-1} and 6 pC N^{-1}, respectively.[96,105] AlN thin films are ideal for resonators and sensors due to their high thermal conductivity and low dielectric and acoustic losses.[106] They are also commonly used in microelectromechanical systems (MEMS) because of their high temperature and humidity stability, as well as their compatibility with CMOS processing.[104] Lithium niobate, with its excellent electromechanical coupling and very high quality factor, is a desirable material for MEMS resonators.[107–109]

The application of piezoelectric materials is primarily confined to actuators and sensors, largely due to their low energy conversion efficiency. In contrast, nanostructured piezoelectric materials have higher energy conversion efficiency, as they can endure greater strain. Moreover, nano-structured materials have higher surface-to-volume ratios, which further enhance their performance.[110] For example, pressure trigger was developed using a zinc oxide (ZnO) piezoelectric fine-wire (PFW), such as a microwire or nanowire, which is activated when subject to an external impact force.[111] By synthesizing ZnO nanorods on conductive textiles, textile-based PEDOT:PSS/CuSCN/ZnO wearable nanogenerators have been fabricated successfully. This has substantial promise for self-powered, soft, electronic devices.[112] In contrast, despite excellent piezoelectric properties, piezoelectric ceramics are typically brittle; this limits their use in energy harvesting applications such as transducers because of their inability to absorb large strains without sustaining damage.[113]

In addition to pure PZT, there are several other piezoelectric materials, such as relaxor ferroelectrics (*e.g.*, PMN–PZT, PMN–PT, and PNN–PZT), which exhibit significantly high piezoelectric properties. The piezoelectric constant (d_{33}) reaches approximately 1530 pC N^{-1} for the ⟨001⟩ single crystal (S-crystal) and 1100 pC N^{-1} for the ⟨001⟩ textured ceramic (T-ceramic) in the $0.4Pb(Mg_{1/3}Nb_{2/3})O_3$–$0.25PbZrO_3$–$0.35PbTiO_3$ (PMN–PZT) composition synthesized by a conventional solid-state reaction method.[114]

Lead magnesium niobate-lead titanate (PMN–PT) [$0.70Pb(Mg_{1/3}Nb_{2/3})O_3$–$0.30PbTiO_3$] is another well-known relaxor ferroelectric that exhibits exceptionally high electromechanical performance with a piezoelectric coupling constant, $d_{33} \approx 2000$ pC N^{-1}, and electromechanical coupling factor, $k_{33} \approx 0.93$, in the single crystal form.[115] These values are nearly 30 times higher than those of $BaTiO_3$ and about four times higher than those of bulk PZT.[116] Furthermore, top-down fabrication method has been used to develop a PMN–PT single-crystal nanobelt functioning as a nanogenerator with an output voltage of 1.2 V.[117]

Rare-earth doping, particularly at the A-site of the perovskite structure, has proven effective in enhancing the piezoelectric properties of relaxor ferroelectric crystals by introducing local structural heterogeneity. For example, Sm-doped $Pb(Mg_{1/3}Nb_{2/3})O_3$–$PbTiO_3$ (Sm–PMN–PT) single crystals with the composition $Sm_{0.01}Pb_{0.985}[(Mg_{1/3}Nb_{2/3})_{0.70}Ti_{0.30}]O_3$ grown using a modified vertical Bridgman method exhibit d_{33} values between 3400 and 4100 pC N^{-1}, showing good uniformity.[115]

However, their relatively low Curie temperature limits their use in high-temperature applications. To address this, Nd^{3+} were introduced to replace Pb^{2+} with the composition $Nd_{0.002}Pb_{0.997}[(Mg_{1/3}Nb_{2/3})_{0.68}Ti_{0.32}]O_3$. The resulting Nd-doped PMN–PT crystals showed piezoelectric coefficients above 3000 pC N^{-1}, making them strong candidates for high-performance piezoelectric transducers.[118]

Another notable example is the $[001]_C$-textured relaxor ferroelectric composition PNN–PZT [$0.55Pb(Ni_{1/3}Nb_{2/3})O_3$–$0.15PbZrO_3$–$0.3PbTiO_3$], which exhibits excellent piezoelectric properties (d_{33} = 1210 pC N^{-1}, d^*_{33} = 1773 pm V^{-1} at 5 kV cm^{-1}). These values were achieved using 2 vol% $BaTiO_3$ platelet templates.[119]

As one of the first piezoelectric polymer materials (see Table 3), semi-crystalline polyvinylidene fluoride (PVDF) was discovered by Kawai in 1969.[19] In semi-crystalline materials, microscopic crystals are randomly oriented and dispersed within an amorphous matrix. These materials will exhibit piezoelectric properties when the micro-crystals reorient after poling.[120] At present, PVDF is the most widely used piezopolymer, given that poled PVDF demonstrates the highest yet observed piezoelectric coupling, ranging from 24 to 34 pC N^{-1} in the β-phase. Due to its flexibility, low acoustic impedance, excellent electromechanical response, biocompatibility, and chemical stability, PVDF is used in a wide range of applications.[121] Examples include wearable piezoelectric energy harvesters and biomedical engineering applications.[122,123]

Unlike pure PVDF, the copolymer PVDF–TrFE (trifluoroethylene) does not require poling to exhibit piezoelectric properties. Although the TrFE units reduce the dipole moment of the PVDF chain due to the addition of a third fluorine atom,[121] the piezoelectric constant of PVDF–TrFE was found to be in the range of 25 to 40 pC N^{-1}.[130] Various methods have been utilized

Table 3 Properties of piezoelectric polymers

Material	d_{33} (pC N^{-1})	g_{33} (V m N^{-1})	k	Y (GPa)	T_C (°C)	Advantages	Limitations
PVDF (semi-crystalline)	24 to 34[124]	0.34[121]	0.20	4.18	75–80	Flexible, stable, low acoustic impedance, excellent response. Used in wearable energy harvesters and biomedical devices	Lack of β phase limits its applications.[125] Narrow operating temperature[126]
PVDF–TrFE (semi-crystalline)	−25 to −40	−0.542	~0.29	~1.5	~110	Advantages over PVDF in fabrication and piezoelectric applications; used in sensors and power harvesters	High processing temperature, limited long-term stability, high cost[127]
Nylon-11 (polyamide) (semi-crystalline)	7.2[128]	—	—	—	—	Harvest energy from movement, used in apparel, health monitoring, sportswear, and portable energy generation[129]	Conventional fabrication does yield piezo nylon; polyamides are hydrophilic
Polyimide (amorphous)	−2.7	0.087	—	—	225	High glass transition temperature, use in MEMS devices	Low piezo constant, time decaying response
Parylene-C (amorphous)	−2[124]	—	0.02[120]	2.8[120]	—	Biocompatibility, stability, low acoustic and mechanical impedance, MEMS	Low piezo constant, low energy harvesting efficiency

to prepare PVDF–TrFE sheets and films and also enhance the piezoelectric properties. These have been developed for applications such as power harvesters, flexible tactile sensors, capacitor-based sensors, touch sensors and actuators.[131–135] However, the induced strain in both PVDF and its copolymers with TrFE is highly dependent on a strong electric field, which significantly compromises their reliability and restricts their practical use in wearable devices.[136]

In addition to PVDF and its various copolymers, piezoelectric effects have also been observed in other semi-crystalline materials, such as polyamides, for example in odd-numbered nylons, such as nylon-11, that exhibits a piezoelectric constant of 7.2 pC N^{-1} in the δ′-phase.[137] This material can play a crucial role in energy harvesting, as well as in smart and wearable electronic textile applications. However, traditional fiber production methods such as melt extrusion and melt spinning produce non-piezoelectric polycrystalline α-phase nylon fibers, limiting the potential applications of piezoelectric nylon-11 in E-textiles.[129]

Polyimides are one of the most important amorphous polymers; their glass transition temperature makes them ideal for high-temperature applications.[138] Although they have a lower piezoelectric constant (−2.7 pC N^{-1}) than that of PVDF, they are usable over a wider temperature range. While the piezoelectric properties of PVDF can deteriorate when exposed to temperatures above 70 °C, polyamides maintain their piezoelectricity up to 150 °C, making them ideal for high-temperature MEMS sensor applications. The first study on parylene-C (PA-C) as a piezoelectric material was conducted in 2011 and the d_{33} value was found to range from −0.01 to −2.00 pC N^{-1}.[124] Due to its biocompatibility and chemical stability, parylene-C (PA-C) is highly suitable for integration into MEMS devices, including sensors and cantilevers. Although piezoelectric polymers are cost-effective, lightweight, and flexible, and offer a simple solution for numerous applications, they do have drawbacks. These include limited mechanical strength, poor thermal stability, low piezoelectric coefficients and low electromechanical coupling coefficient. The combination of all of these leads to poor energy harvesting capabilities.

Alternatively, piezoelectric composite materials (Table 4) combine the desirable properties of ceramics with the flexibility of polymers offering the advantages of both materials. The concept of piezoelectric ceramics/polymer composites was first introduced in the 1970s by Newnham.[121] Piezocomposites have higher coupling properties and dielectric constant of ceramics, along with the mechanical flexibility and low acoustic impedance of polymers. The polymer in the composites can be either piezoelectric or non-piezoelectric.[102] For instance, polydimethylsulfide (PDMS) lacks intrinsic piezoelectric properties, but it can still be used as a polymer matrix in composites because of its flexibility, thermal stability, and chemical durability.

One of the most widely used piezocomposites is PVDF–PZT. Pure PZT exhibits high impedance, rigidity, brittleness, and inflexibility,[139] while PVDF has low piezoelectric coefficient and low stiffness. Individually, these attributes limit possible

Table 4 Properties of composite piezoelectric materials

Material	d_{33} (pC N^{-1})	g_{33} (V m N^{-1})	Y (GPa)	Advantages	Limitations
PVDF–PZT (30–70)	35.8[140]	—	0.894–1.725[140]	Softer than PZT, used in force sensor, self-powered sensor for real-time monitoring of sport activity	Uneven mixing of fillers in the matrix, small mechanical force transmission to the piezoelectric particles, and low polarization efficiency
$BaTi_{0.3}$/PVDF (60–40)	28	0.16[142]	35[143] (with 50 vol% of $BaTiO_3$)	Self-powered wearable electronics, actuators and energy harvesting	
BCZT with PDMS	31[146]	0.6[146]		Low-power wearable and portable electronic devices. Energy supplies for implantable biomedical devices	
ZnO–CNF	9.49[125]			Energy harvesting and environmental monitoring	
ZnO–CNF–PVDF	31 ± 2.07[125]			Excellent flexibility, self-powered wearable electronic devices	

applications. However, by combining PVDF and PZT in a composite, the electromechanical and mechanical properties can be significantly enhanced. Using a 3/7 fraction ratio, the PVDF–PZT composite has d_{33} = 35.8 pC N^{-1}, greater than that of pure PVDF (18.3 pC N^{-1}). Such composite films are suitable for small force sensor applications.[140] Remarkably, a self-powered PZT/PVDF piezoelectric sensor has been developed for real-time monitoring of table tennis training.[141]

A lead-free piezocomposite has been developed by dispersing BT ceramic grains into a PVDF matrix. The piezoelectric constant for the 0.6$BaTiO_3$/0.4PVDF composite was found to be 28 pC N^{-1}, which was increased to 61 pC N^{-1} when $BaTiO_3$ nanowires with 50 vol% of $BaTiO_3$ were dispersed into 5.5 wt% of a PVDF polymer matrix.[142] Due to mechanical flexibility and relatively high dielectric constants, this composite has significant potential for use in wearable electronics.[143–145] Additionally, BCZT/PDMS piezocomposites have achieved g_{33} = 0.6 Vm N^{-1}, the highest value recorded so far in piezocomposites. This promises significant potential applications for wearable electro-mechanical technologies.[146]

Other composites have been developed by loading cellulose nanofibers (CNF) with ZnO to form CNF/ZnO composites, which exhibit a piezoelectric constant of 9.5 pm V^{-1}. This value can be further increased to 25 pm V^{-1} (with $d_{33} \approx$ 31 pC N^{-1}) by incorporating PVDF into the composite, resulting in the PVDF/CNF@ZnO (E-PVDF/CZ) composite. A flexible piezoelectric sensor was developed for applications in energy harvesting and environmental monitoring.[125]

Traditional polymer–ceramic piezocomposites often suffer from poor stress transfer between the polymer matrix and ceramic fillers, thereby limiting their energy harvesting capabilities. To overcome this, a biofibril template method was used to develop a 3D Sm-doped PMN–PT ceramic skeleton, which was then embedded in a flexible polymer matrix. The resulting piezocomposite exhibits significantly enhanced performance, achieving an open-circuit voltage of approximately 60 V and a short-circuit current density of ~850 nA cm^{-2}, with a peak instantaneous power density of ~11.5 μW cm^{-2} which is about 16 times greater than that of the traditional nanoparticle-based composites.[147]

Piezoelectricity can also be observed in porous charged polymers, commonly referred to as ferroelectrets, discovered in the 1990s by Kirjavainen.[148] Different polymers such as polypropylene (PP), poly(ethylene terephthalate) (PET), poly(ethylene naphthalate) (PEN), poly(tetrafluoro ethylene) (PTFE), cross-linked PP (XPP), and some cyclo-olefines have been considered for different cellular films (see Table 5). Ferroelectrets have a wide range of applications due to their high piezoelectric constants, low cost, flexibility and low specific weight.[149] Cellular polypropylene (PP) is a significant ferroelectret exhibiting d_{33} = 1.2 nC N^{-1} for a single layer. This response can be further multiplied by using multilayer films. The material performs well in fatigue resistance, stiffness and charge-trapping properties.[150] Cellular PP has been used in pressure sensing applications such as touch pads, accelerometers, long-term respiration monitoring due to their good sensitivity and

Table 5 Properties of cellular piezoelectric materials

Material	d_{33} (pC N^{-1})	g_{33} (V m N^{-1})	Y (GPa)	Advantages	Limitations
Semi-crystalline cellular polypropylene (ferroelectrets)	130–2100	30	0.002	Low cost, good fatigue resistance, used in microphones, transducers and accelerometers	Limited long-term and thermal stability, electrets tend to gradually lose polarization at higher temperatures
PDMS with polar nanoparticles	37 (d_{31})[157,158]		1.5[159]	Stretchable sensors, energy harvesting, soft robotics, and flexible electronics	
Soft composite fiber mats (BT + PLA)[160,161]	~1000		~0.0001	Lightweight, biocompatible, application in active implants, artificial muscles, sensors, textiles	

capability for self-power.[151,152] Cross-linked PP ferroelectret films exhibit d_{33} as large as 230 pC N^{-1}. These films can be utilized to harvest sound energy by being applied to the inner walls of cavities in Helmholtz resonators, making them ideal for applications in road transport and high-speed railways.[153] Polyester ferroelectrets, such as polyethylene terephthalate (PET) foams and polyethylene naphthalate (PEN), demonstrate piezoelectric coefficients of 500 and 140 pC N^{-1}, respectively, while maintaining stable sensitivity up to 80 °C.[149]

Ferroelectrets have emerged as promising materials for a broad spectrum of applications, including tactile sensors, accelerometers, gaming, robotics and force myography (FMG) which detect body motion. This is attributed to their exceptional piezoelectric coefficients, low elastic moduli, high flexibility, and notable stretchability.[124,154–156] Despite their advantages, ferroelectrets face several challenges, primarily related to limited long-term and thermal stability. Overcoming these limitations could significantly enhance their performance and broaden their scope of application in various fields.

Highly piezoelectric biocompatible soft fibers were created by dispersing BT ceramic particles into electrospun polylactic acid (PLA). The strongest converse piezo response was observed when the BT particles were uniformly aligned and poled within the fiber, resembling ferroelectret polymer foams. This response was an order of magnitude greater than that seen in single-crystal BT films. These mats, due to the PLA's biocompatibility, have potential applications in biological fields such as biosensors, artificial muscles, and energy harvesting devices.[160,161]

Piezoelectricity has also been explored in various biomaterials (Table 6), including collagen, DNA, bone, cellulose, and amino acids.[14,162,163] The piezoelectric constant of bone was measured to be 0.2 pC N^{-1}.[164] It was found that piezoelectricity in collagen contributes to the piezoelectric effect observed in bone.[164,165] The piezoelectric constant for type I collagen fibrils in both murine and bovine Achilles tendons was found to be in the range of 1–2 pm V^{-1},[166,167] while for *D*-periodic reconstituted collagen fibrils, the value was 1.6 pm V^{-1}.[168]

The piezoelectric effect in DNA films, particularly due to shear and hydration effects, has also been studied, though the origin remains unclear and the quantitative values are poorly determined.[169] Non-chiral amino acid glycine demonstrates a piezoelectric response, with β-glycine and γ-glycine having piezoelectric coefficients of 6 pm V^{-1} and 10 pm V^{-1}, respectively.[169] In cellulose nanofibers (CNFs), piezoelectric force microscopy (PFM)[125] provided d_{33} = 5.9 pm V^{-1}, while d_{33} = 0.4 pm V^{-1} for pure wood cellulose. In spite of this, cellulose can be incorporated into piezoelectric composites as a functional filler to enhance performance.[170] Beyond natural materials, the piezoelectric properties of the M13 bacteriophage have also been studied, showing a response of up to 7.8 pm V^{-1}. A phage-based piezoelectric generator has been developed, capable of generating up to 6 nA of current and 400 mV potential, which can be used to power liquid crystal displays (LCDs). These viral particles, along with other biomaterials, show significant potential for application in energy storage, generation, and tissue regeneration.[171]

Table 6 Piezoelectric properties of biomaterials

Materials	d_{33}(pC N^{-1})	Young's modulus (MPa)	g_{33} (V m N^{-1})	Advantages	Limitations
Collagen fibres[168]	~1–2			Important for tissue engineering applications	Low piezoelectric coefficients limit technological applications
M13 bacteriophage[171]	7.8				
DNA[172]	Not known				
Bone[173]	0.2				
β-Glycine (amino acids)[169]	6	15	8.13		
γ-Glycine[169]	10	28	0.46		
Cellulose	0.4[170]				
Cellulose nanofibers (CNF)	5.85[125]				

III.B. Smectic and columnar liquid crystals (1-D and 2-D solids)

Smectic liquid crystals have a one-dimensional layered structure, while columnar liquid crystals form a structure ordered in two directions and fluid in the third. These can be described as one- or two-dimensional solids, respectively. Such symmetries, in some cases, allow linear couplings between the electric field and the mechanical strain, *i.e.* piezoelectricity. A schematic of possible molecular packing, their respective symmetry groups (using Schönflies notations), and the non-vanishing piezoelectric coefficients for known smectic liquid crystals is shown in Fig. 4.

The SmA* phase (see Fig. 4(a)) has D_∞ symmetry, *i.e.*, complete rotation symmetry along the long molecular axis but without a mirror plane (due to the molecular chirality). In this phase, shear along the smectic layers (indicated by light magenta planes) by stresses T_{12} or T_{13} results in electric polarization along axis 3 or 2, respectively. This yields non-zero $\gamma_{3,12}$ (= $-\gamma_{2,13}$) piezoelectric coupling coefficients. Such an effect was tested and measured in the SmA* (L_α) phase of phospholipid L-α-phosphatidylcholine, which is often considered as a model for bilayer cellular membranes.[174] The underlying physical mechanism was postulated to be mechanical shear (T_{12} or T_{13})-induced tilt of the average molecular orientation (director) with respect to the layer normal, which leads to a shear-induced SmC* configuration (see Fig. 4(b)) with polarization normal to the tilt (shear) plane.[50,175] The induced polarization was found to be proportional to the induced tilt angle with a coefficient of ~60 nC cm^{-2} degree^{-1}. Cell membranes made up from lipid bilayers also have SmA* structure, suggesting that cell membranes should also be piezoelectric. The piezoelectric origin of the effect was confirmed by studies comparing non-aqueous lamellar phases of left-handed (L_α-phosphatidylcholine), right-handed (D_α-phosphatidylcholine) and racemic (DL-alpha-phosphatidylcholine) lipids.[176]

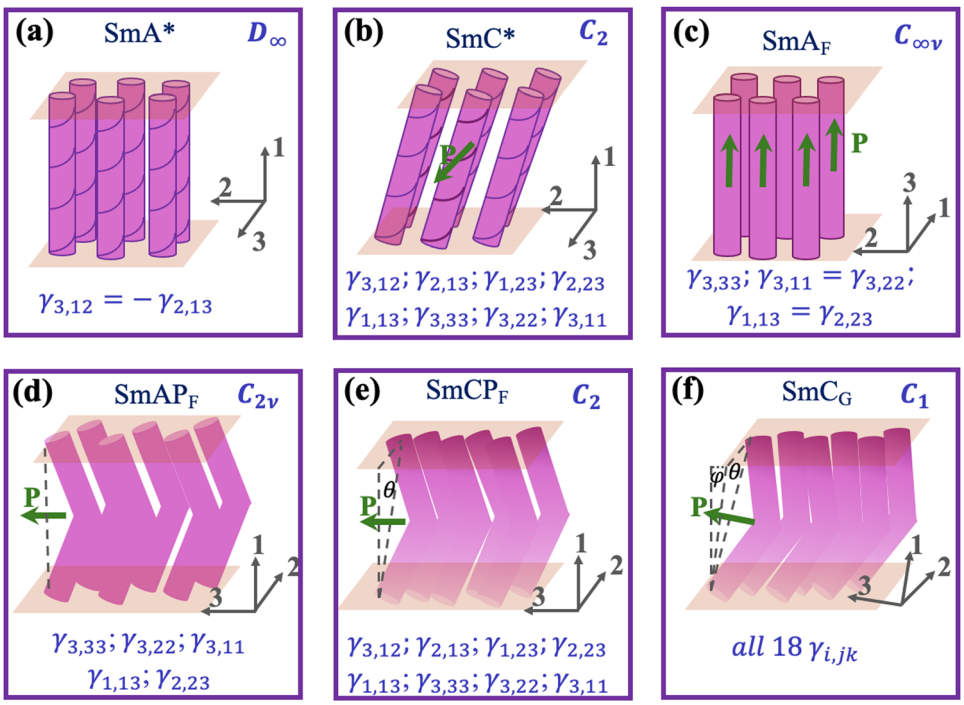

Fig. 4 Sketch of the molecular packing, their symmetry using Schönflies notations, and the non-vanishing piezoelectric coefficients determined by the Curie-principle for known non-centrosymmetric smectic liquid crystals: (a) SmA*, (b) SmC*, (c) SmA_F, (d) $SmAP_F$, (e) $SmCP_F$ and (f) SmC_G phase.

It was further hypothesized that electric charge separation can be induced along membranes when the lipids become tilted as a result of mechanical stimuli. Importantly, tilt-induced polarization occurs within the insulating chains of the bilayers, and therefore, cannot be screened by free ions of the surrounding aqueous plasma. It has been suggested that cell membrane piezoelectricity may be utilized in mechanoreceptors; and can even explain that some species (*e.g.* pigeons and turtles) can navigate without visual reference. In some cases, animal cells contain magnetite (Fe_3O_4) nanoparticles that form chains and act as compass needles to sense local changes in the magnetic field.[177,178] Although magnetoreception of migratory animals is well established experimentally, its biophysical mechanism is not yet clear. The chains of these magnetite nanoparticles are connected to the cell membranes *via* nanofibers, thus exerting shear stress on the cell membrane when the compass needle moves. Piezoelectric coupling of cell membranes, as explained above, suggests that a shear-induced electric signal may open ion-channels embedded in the cell membrane and thus trigger much larger electric signals that depend on the position of the ion channel and the shear-induced polarization. This may provide both orientational and positional information necessary for navigation.

The converse piezoelectric effect in SmA* leads to a shear strain in 1–2 planes due to an electric field applied in the perpendicular direction. Such shear strain is expected to lead to a tilt of the director. The optical consequence of this effect, rotation of the optic axis (the director) proportional to the electric field, has been indeed observed, and is known as the electro-clinic effect.[179] Spillmann *et al.* studied SmA* elastomers and found an electric field-induced twist whose direction changes sign with that of the electric field.[180] The sense of the twist is controlled by the chirality, just as the direction of the tilt in the electro-clinic SmA* materials.

Piezoelectric effects have been studied experimentally largely in the SmC* phase (see Fig. 4(b)). SmC* is the first liquid crystal phase that was found to be ferroelectric.[50,51] As argued by Meyer, the ferroelectric polarization is along the smectic layers perpendicular to the tilt plane due to the combined effect of the director tilt and chirality. Without director tilt, the material would be SmA*, where an electric polarization along the layers would be canceled due to continuous symmetry axis normal to the layers. This symmetry would allow for a 180° rotation along the director that would cancel any vector response within the layer, as illustrated in Fig. 5(a). As we discussed above, in spite of the lack of ferroelectricity, this phase is piezoelectric. A director tilt without molecular chirality also would not allow for polarization within the smectic layers, as illustrated in Fig. 5(b). This phase has a C_{2v} symmetry, *i.e.*, a two-fold rotation normal to the tilt plane, as such rotation would not change the structure. This 180° rotation would allow for the existence of a vector normal to the tilt plane. However, the SmC phase also has a mirror symmetry in the tilt plane (this is expressed by the v in the subscript), which would negate a vector normal to the tilt plane. The SmC* phase lacks both rotation symmetry along the director and the mirror plane

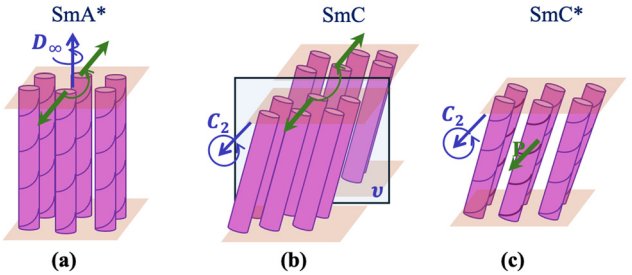

Fig. 5 Illustration of Meyer's arguments explaining the existence of polarization in chiral smectic C* liquid crystals. (a) SmA* has D_∞ symmetry: an infinite fold rotation along the director (smectic layer normal) that includes a 180° rotation, which would turn any vector along the smectic layer to an opposite direction. (b) Non-chiral SmC phase has C_{2v} symmetry, including a two-fold rotation normal to the tilt plane and a mirror plane along the tilt plane that rotates a vector normal to the tilt plane into an opposite direction. (c) Chiral smectic C* (SmC*) phase has only a two-fold rotation (C_2) symmetry axis normal to the tilt plane, allowing the existence of a non-zero vector (such as spontaneous polarization) normal to the tilt plane.

along the tilt plane, thus allowing a non-zero polar vector, such as the electric polarization normal to the tilt plane (see Fig. 5(c)). Such a situation is often expressed as tilt + chirality → polarity. As can be seen in Fig. 4(b), there are 8 piezoelectric constants in SmC* with a C_2 symmetry that can be non-zero. Those are the terms where the coordinates (1 and 2) normal to the electric polarization vector (3) appear either twice or together.[181] This is because an inversion of coordinates 1 and 2 (which is allowed by symmetry) will change the sign of the coupling constant, so two of them must be done simultaneously.

Fig. 4(c) shows the structure of a polar smectic A (SmA_F) phase with polarization direction along the director of achiral rod-shape molecules with high molecular dipole moments. Such phase just has been observed recently among materials that also form the 3D fluid ferroelectric nematic (N_F) liquid crystal phase.[182,183] The symmetry and the possible piezoelectric couplings of this phase is the same as that of the N_F phase and is discussed subsequently. Due to the very recent observation of this phase, no experimental confirmation of its piezoelectric response is yet available.

Fig. 4(d–f) show the structures, symmetries and possible piezoelectric coupling constants of achiral bent-shaped molecules forming smectic phases.[53,182,184–187] It is noteworthy that the $SmCP_F$ phase has the same C_2 symmetry and the same 8 possible piezoelectric coupling constants as of the SmC* phase. Furthermore, the double-tilted SmC_G phase is the least symmetric 2-dimensional fluid phase,[184,187,188] which has only C_1 symmetry that allows for all 18 possible piezoelectric coupling constants.

Experimentally, the first observation was a direct piezoelectric response, *i.e.*, shear-induced polarization.[189,190] It arises from the distortion of the helix, as illustrated in Fig. 6. In the ground state (no-shear, Fig. 6a), the director, which is tilted with respect to the layer normal by an angle θ, forms a helix having the chiral pitch, p; p is typically in the micron range. Consequently, the spontaneous polarization is rotated in

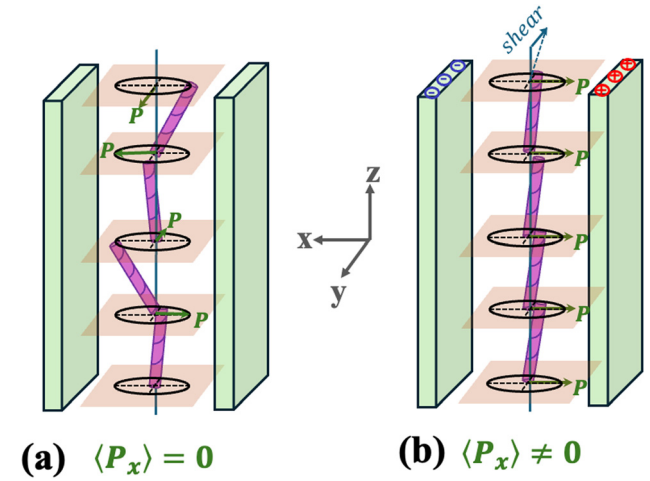

Fig. 6 Illustration of the shear deformation of the director structure and the induction of net polarization in the SmC* phase. The smectic layers are parallel to the x–y plane. The tilt plane rotates from one layer to the other. (a) Undisturbed helical structure where the macroscopic polarization is averaged out. (b) Due to the action of the shear along y, the axial symmetry of the configuration is broken, and a non-zero polarization component appears along x. Arrows indicate the spontaneous polarization $\vec{P}$, which is normal to the tilt plane (the plane determined by the layer normal and the projection of the tilt direction, the so-called c-director).

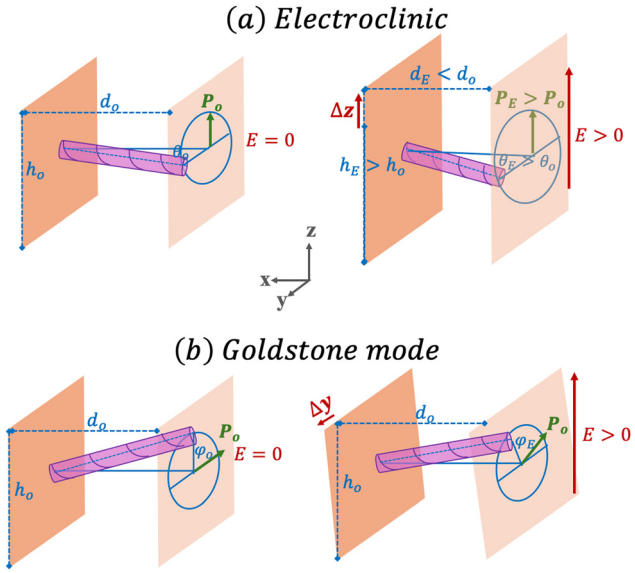

Fig. 7 Illustration of the linear electromechanical effect of SmC* materials due to the electroclinic effect (a) and the backflow related to the Goldstone-mode director rotation (b).

subsequent layers[50] but will average to zero over distances greater than p.

The shear in the yz plane aligns the projection of the c-director (the projection of $\hat{n}$) onto the layer plane parallel (and consequently the polarization normal) to the shear plane, leading to $\langle P_x \rangle \neq 0$, as shown in Fig. 6(b). Ferroelectric chiral SmC* elastomers can also be piezoelectric. However, so far their direct piezoelectricity was only considered theoretically by Adams and Warner.[191] Direct piezoelectric effects were also observed in lyotropic liquid crystals and in membranes with C_2 symmetry.[192]

Converse piezoelectric responses in SmC* materials have also been studied since 1985.[49] A systematic study with accurate control of the alignment revealed that induced motion parallel to the smectic layers (and the film surface) is generally the strongest, especially if the polarization is also parallel to the plates.[42] Motion normal to the film substrates is due to the electro-clinic effect that causes a field-induced variation of the tilt angle that results in a change in the layer spacing. When the polarization is parallel to the field, the tilt angle (consequently the value of the polarization) increases and the layer spacing decreases. When the polarization is opposite to the field, the tilt angle decreases and the layer spacing increases. Since the number of layers cannot change in short time, the variation in the layer spacing results in a force normal to the cover plate and a variation in the film thickness (see Fig. 7(a)).

Motion along the film surfaces (shear strain) is related to "backflow",[193] *i.e.*, to the coupling between the gradient of the director rotation about the layer normal (Goldstone mode[194]) and the flow field. This mode is excited by the electric field *via* the torque $\vec{E} \times \vec{P} = E{\cdot}P{\cdot}\sin\Phi$, where Φ is the angle between the electric field and the spontaneous polarization. The magnitudes of piezoelectric oscillations are therefore largest when the polarization is parallel to the film surface and perpendicular to the applied electric field (see Fig. 7(b)). Typically, piezoelectric coupling constants in the SmC* phase are in the order of 50 pC N^{-1}, which is comparable to solid piezoelectric materials.

In addition to bulk thermotropic SmC* materials confined between glass plates, converse piezoelectric-type responses were also observed in free-standing ferroelectric SmC* films subject to AC electric fields applied along the film surface.[195–197] Additionally, this was observed in lyotropic liquid crystals.[192] Finally, the converse piezoelectric effect has also been reported in SmC* glasses[198] and elastomers[199] that can sustain strain in all three directions.

Experimentally, only one piezoelectric coupling constant has been determined in the synclinic tilted polar ferroelectric SmC_sP_F phase (molecules are tilted in the same direction in subsequent layers) with $P_o \approx 5$ mC m^{-2} polarization by testing the converse piezoelectric responses in two directions. It was found that $\gamma_{3,33} \approx 2\gamma_{3,22} \approx 100$ nC N^{-1}.[200]

The candidate molecular structures, symmetries and allowed non-zero piezoelectric constants of columnar liquid crystals (2-D solid materials) are shown in Fig. 8. Fig. 8(a) shows the tilted chiral columnar (Col_t^*) phase[52] with a C_2 symmetry and 8 possible piezoelectric coupling constants. Fig. 8(b) illustrates the hexagonal pyramidal $(\mathrm{P_h})$ phase of achiral bowl (pyramidal)-shaped molecules with C_{6v} symmetry and 3 possible (2 independent) non-zero piezoelectric constants. Fig. 8(c) represents the chiral hexagonal pyramidal shape $(\mathrm{P_h^*})$ phase with a C_6 symmetry and 3 independent possible non-zero piezoelectric constants. Finally, Fig. 8(d) shows the tilted pyramidal (P_t) phase of achiral bowl (pyramidal)-shaped molecules with C_{1v} symmetry and 3 possible (2 independent) non-zero piezoelectric constants.

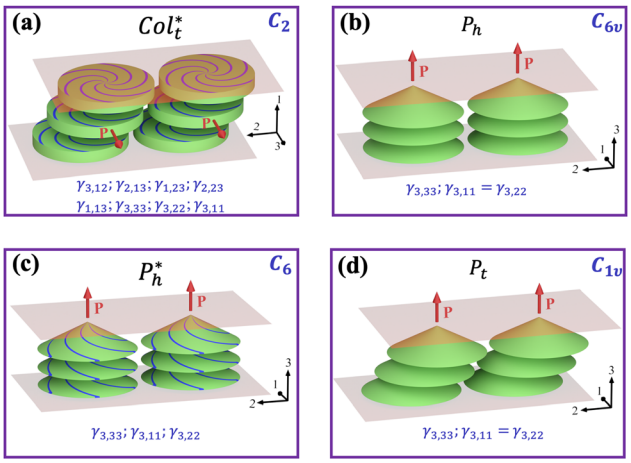

Fig. 8 Molecular structures, symmetries and possible non-zero piezoelectric constants of columnar liquid crystals (2-D solid materials). (a) Tilted chiral columnar (Col_t^*) phase with C_2 symmetry and eight possible piezoelectric coupling constants. (b) Hexagonal pyramidal (P_h) phase of achiral bowl (pyramidal)-shaped molecules with C_{6v} symmetry and three possible (two independent) non-zero piezoelectric constants. (c) Chiral hexagonal pyramidal shape (P_h^*) phase with C_6 symmetry and three independent possible non-zero piezoelectric constants. (d) Tilted pyramidal (P_t) phase of achiral bowl (pyramidal)-shaped molecules with C_{1v} symmetry and three possible (two independent) non-zero piezoelectric constants.

The ferroelectric Col_t^* columnar liquid crystal 1,2,5,6,8,9,12,13-octakis[(*S*)-2-heptyloxy]dibenzo[*e*,*l*]pyrene (D8m*10)[201] has demonstrated converse piezoelectric effects.[40] A piezoelectric coupling constant $\gamma_{3,33} \sim 1$ pC N^{-1} is reported; this is 1000× less than what is typical in SmC* materials.

III.C. Liquid crystals lacking spatial order (3-D liquids)

Nematic (N) and chiral nematic (or cholesteric; N*) liquid crystals are fluid in three directions, *i.e.*, their long-range order is purely orientational (no positional order). The N phase has an inversion symmetry and as such does not allow piezoelectricity. The N* has the same D_∞ symmetry along the director, as does SmA*, so only the $\gamma_{1,23} = -\gamma_{2,13}$ piezoelectric coefficients (see Fig. 4(a)) may be non-zero. However, the optical axis of N* follows a helix, so that all piezoelectric coefficients average to zero over a distance greater than the helix pitch, which typically is 0.1 μm $< p <$ 100 μm.[75] To date the only reports of piezoelectricity in N* are in polymerizable materials where crosslinked chiral molecules produce an unwound N* elastomer.[202,203] In this case, while there is no long-range positional order, cross-linking severely restricts molecular motion, resulting in the ability to sustain elastic strain.

Fluid liquid crystals with a ferroelectric nematic (N_F) phase[54–59,204] represent materials combining true 3D fluidity with a polar order. That is, true fluid materials lack the inversion symmetry; this allows several piezoelectric couplings. The N_F phase has a $C_{\infty v}$ symmetry, *i.e.*, a continuous rotational symmetry about the polar axis and a mirror symmetry through any plane containing the polar axis. This means that any reflection through the 1–3 (or 2–3) plane changes the sign of 2 (or 1); therefore, the components of $\gamma_{i,jk}$ containing an odd number of either 1 or 2, must be zero. Thus, the non-vanishing piezoelectric tensor elements are $\gamma_{3,33}$, $\gamma_{3,11}$ (= $\gamma_{3,22}$) and $\gamma_{1,13}$ (= $\gamma_{2,23}$ = $\gamma_{1,31}$ = $\gamma_{2,32}$). The depictions of non-zero coupling constants in converse piezoelectric effects are shown in Fig. 9.

By controlling the geometry, *i.e.*, the alignment direction in the N_F phase and the direction of the applied electric field, various components of γ can be determined. For example, with electrodes on the top and bottom of a thin film (parallel plate capacitor geometry) and the director aligned perpendicular to these plates, $\gamma_{3,33}$ can be measured by detecting film thickness variations induced by the electric field. In order to discriminate between converse piezoelectricity and other non-linear (higher harmonic) electromechanical effects, one typically uses a

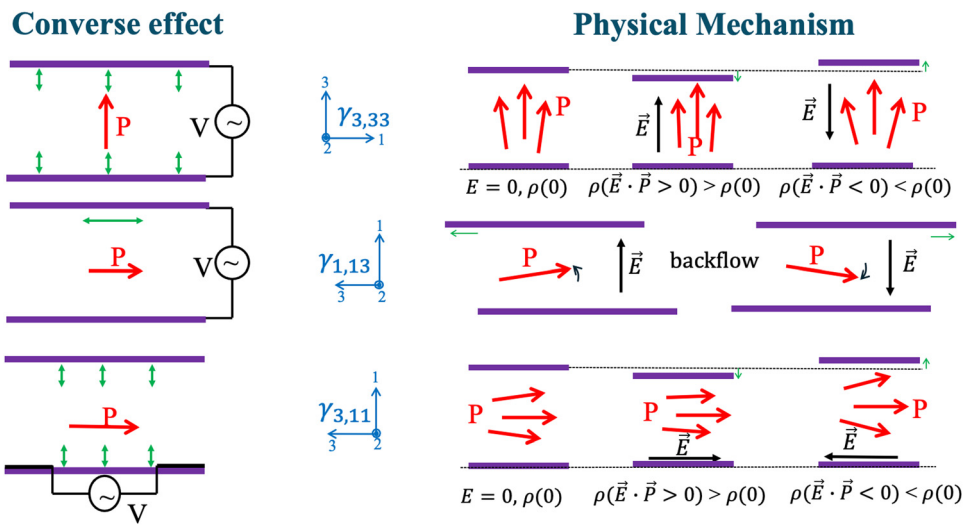

Fig. 9 Depictions of non-zero coupling constants (left) in converse piezoelectric effects and the proposed physical mechanisms (right) corresponding to those coefficients. In each illustration, black arrows and circuit elements represent the stimulus (electric field or applied voltage), green double-headed arrows show the response (mechanical vibration), and red arrows show the direction of the spontaneous polarization.

sinusoidal electric potential and phase-sensitive detection to assure that only motion having the same frequency is sampled.

In contrast to $\gamma_{3,33}$, $\gamma_{1,13}$ can be measured with the voltage applied between the electrodes when the material in N_F phase is aligned parallel to the substrate. For the measurements, the motion detector (which usually is an accelerometer, as described in Section 2.2) should detect the vibration of the top plate parallel to the rubbing direction of the alignment layer.

The third non-zero coupling constant, $\gamma_{3,11}$, can be measured with the director aligned parallel to the substrate, and using an in-plane electric field in the same direction; in this case, motion normal to the substrate must be determined.

The physical mechanisms leading to the mechanical displacements allowed by the non-zero coupling coefficients are illustrated on the right side of Fig. 9. Specifically, when the ferroelectric nematic material is subject to an electric field parallel to the polarization, fluctuations of the polar order are suppressed, leading to both an increased polarization and closer intermolecular packing, resulting in a greater mass density: $\varrho(E) > \varrho(0)$. Since the ferroelectric nematic materials are incompressible, greater density implies a lesser total volume, so that the boundary surfaces experience a force towards each other. Reversing the sign of the applied electric field will result in a decreased polar order and decreased mass density $\varrho(-E) < \varrho(0)$, which will cause the thickness to increase. This effect is limited to applied electric fields below the coercive threshold. Thus, by measuring the vertical boundary plate motion at the frequency of the applied electric field, we can determine the value of $\gamma_{3,33}$.[193]

The vertical vibration of a planar aligned N_F material upon in-plane electric field corresponding to $\gamma_{3,11}$ has the same field-induced density variation mechanism as that of $\gamma_{3,33}$ (see right-bottom part of Fig. 9). It is important to emphasize that in all converse piezoelectric measurements in the N_F phase, the applied small electric field should not cause significant rotation and realignment of the director. The horizontal vibration of the boundary plate in the $\gamma_{1,13}$ geometry might be due to the backflow,[193] *i.e.*, the coupling of the flow to the inhomogeneous director rotation, as illustrated in the right – middle part of Fig. 9.

Máthé *et al.*[64] explored converse piezoelectricity in N_F materials by measuring the vertical vibration of room-temperature ferroelectric nematic mixtures from Merck, FNLC 1571 and FNLC 919. The coupling constant calculated from the measured displacements was found to exceed 1 nC N^{-1} at frequencies below 6 kHz, which is comparable to values found in both cellular polymers (ferroelectrets)[21–24] and soft composite fiber mats.[160,161] We note that in these measurements, the alignment was not homeotropic but actually pre-tilted, *i.e.*, closer to planar. As explained in Fig. 9, a strictly planar alignment should yield zero displacement. Therefore, it was surmised that the effect measured is in fact due to the small alignment component along the homeotropic direction. This implies that the actual value of $\gamma_{3,33}$ is substantially greater than the quantity measured. To measure the real $\gamma_{3,33}$ coupling constant, one needs to achieve and maintain homeotropic alignment. Unfortunately, the depolarization field[205] present in any N_F material renders perfect homeotropic alignment rather difficult to achieve in practice.

Herein, we report the first measurement of $\gamma_{1,13}$. This requires uniform planar alignment, electric field perpendicular to this alignment, and measurement of the motion along the alignment direction (see Fig. 9). Additionally, we measured the motion in the other two orthogonal directions: normal to the substrates (z-axis) and along the substrate perpendicular to the rubbing direction (y-axis).

According to the symmetry considerations and the proposed physical mechanism shown in Fig. 9, motion in these two directions should be forbidden. We use sinusoidal electric excitation having frequency f and measure the induced accelerations at the same frequency. Thus, the speed of the induced motion will be $v(f) = \frac{a(f)}{2\pi f}$. This is shown in Fig. 10 for a 50 μm cell filled with a room-temperature ferroelectric nematic mixture KPA-02.[206] Upon cooling, KPA-02 exhibits an isotropic-to-N_F phase transition at 47 °C, whereas upon heating it becomes isotropic at 56 °C. The N_F phase is stable below room temperature and its polarization is $P_o \approx 0.045$ C m^{-2} at room temperature.

The largest response is indeed found along the x-axis, where the frequency dependence of the speed is relatively smooth. From the definition of the piezoelectric coupling constant, its magnitude can be expressed as $\gamma = \frac{S}{E}$, where $S = \Delta x/L$ is the strain and $E \approx \frac{U}{L}$ is the applied electric field. This yields $\gamma_{1,13} = \frac{\Delta x}{U} = \frac{v_x}{2\pi f U}$. In Fig. 10, we see that up to $f \sim 1$ kHz v_x is proportional to f and $\gamma_{1,13} \sim 3$ nm $V^{-1} = 3$ nC N^{-1} is nearly constant. At ~6 kHz, $\gamma_{1,13} \sim 0.8$ nm $V^{-1} = 0.8$ nC N^{-1}, and it roughly decreases inversely proportional to the frequency. These values are larger than of the strongest piezoelectric crystals (see Table 2), and comparable to that of soft ferroelectrets.[21–24] This is arguably due to the softness of the fluids

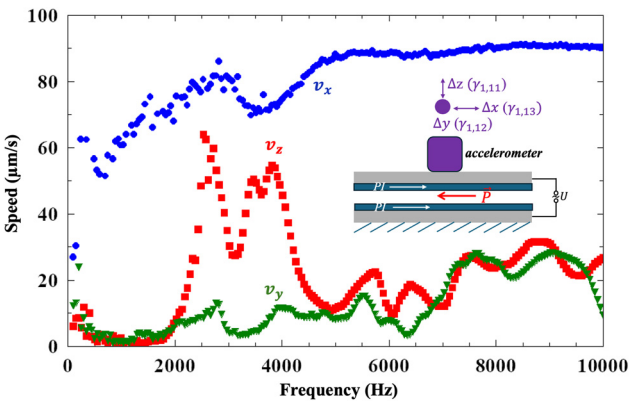

Fig. 10 Frequency dependence of the speed of the top movable plate of a 50 μm cell filled with a ferroelectric nematic mixture KPA-02 at room temperature. The inset shows the geometry and the choice of coordinate system in the measurements.

with loss moduli $G'' = \eta \cdot \omega$, where $\eta \sim 0.1$–1 Pa s is the typical flow viscosity of the FNLC materials. At $f = 6$ kHz $G'' \sim 10^4$ Pa, *i.e.*, hundred thousand times smaller than typical crystalline moduli. This effect, combined with the 10× smaller polarization of ferroelectric nematic fluids than that of crystalline ferroelectrics, provides a context for the larger effective piezoelectric constants of ferroelectric nematic liquids than that of typical ferroelectric crystals. It also explains why at high frequencies, we find $\gamma_{1,13} \propto \omega^{-1}$ for the N_F fluids. Finally, we note that the measured $\gamma_{1,13}$ values may be smaller than the real values, as in our analysis we assumed that the ferroelectric polarization is completely aligned, which maybe far from the case. Although experiments carried out in thin films show that the ferroelectric polarization aligns antiparallel to the rubbing direction,[207,208] this alignment may be less effective for thick films. In the 400–2000 Hz range, the movement along the other two axes is vanishingly small. This is expected as the motion along z and y would involve $\gamma_{1,11}$ and $\gamma_{1,12}$ which are zero by symmetry. Nonetheless, we detect relatively large motion along z as seen by peaks around ∼2.6 kHz and ∼3.8 kHz frequencies. These peaks appear to be related to the bending mode of the top glass plate.[42] The higher frequency mode is apparently related to the bending with respect to the y direction of the glass plate, thus leading to a decrease in motion in the x direction. Other smaller peaks at higher frequencies are either higher harmonics or are coupled to other elastic elements of the sample. The response in the y direction includes smaller peaks mainly correlated with those in the z direction. The responses in the z and y directions could be related to the imperfect alignment and the fact that the top plate is not exactly parallel to the bottom one; therefore, motion in the x direction is coupled to vertical motion. Additionally, the accelerometer has up to 2% cross-talk, *i.e.*, a small fraction of the horizontal motion is picked up by the accelerometer aligned in the other two directions.

As found by Máthé *et al.* for FNLC 1571 and FNLC 919,[64] temperature-dependent measurements show that the converse piezoelectric response exists only in the ferroelectric nematic phase. The temperature dependence (for both increasing and decreasing temperature) of the induced oscillation amplitude $A_x(f) = \dfrac{a(f)}{(2\pi f)^2}$ of KPA-02 is shown in the main panel of Fig. 11 for a 50 μm-thick film subject to 3 V_{rms}, at a frequency of 3 kHz.

The inset shows the voltage dependence of $A_x(f)$ at 25 °C and 3 kHz. Within the measurement error, the voltage dependence is linear for electric potential below 5 V. This is expected for small fields ($E < E_l$) that do not cause large director rotation and realignment. The magnitude of E_l increases with frequency, as discussed by Máthé *et al.*[64]

A direct effect, related to piezoelectricity, called viscous mechano-electric response, was explored by Rupnik *et al.*[65] They employed a room-temperature FNLC 1571 material in the 1–200 Hz frequency range using a simple demonstrator device. A mechano-electric response (mechanical deformation-induced electric signal) was observed when the ferroelectric nematic liquid was placed into a deformable container with

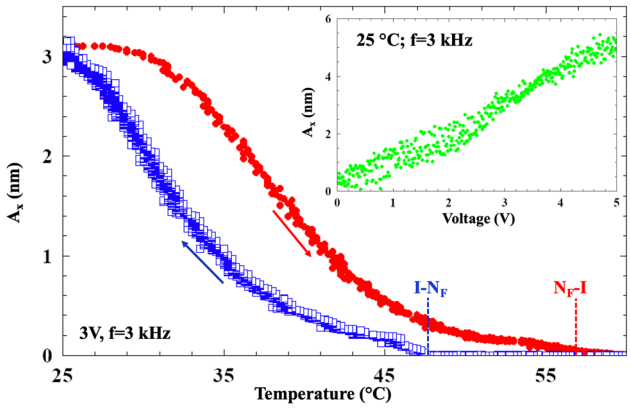

Fig. 11 Temperature dependence of the amplitude of the periodic vibration along the director of a 50 μm KPA-02 film at 3 V and 3 kHz electric voltage during heating and cooling. Inset: Voltage dependence of A_x measured at 3 kHz at 25 °C.

electrodes, and the electric current induced by both periodic and irregular actuation of the container was examined. The experiments reveal several distinct viscous mechano-electric phenomena, where both shape deformations and material flow cause changes in the electric polarization structure of a ferroelectric nematic liquid. The results show that the mechano-electric features of the material promise a considerable applicative perspective spanning from sensitive tactile sensors to energy-harvesting devices. Although the authors did not measure the piezoelectric coupling constant, they estimated the theoretical limits of the electric energy generation of ferroelectric nematic materials. They found that 100 Hz actuation frequency and 100 kΩ load resistance may generate ∼0.1 W cm^2 power per unit area, which is comparable to the specific power produced by solar photovoltaic panels under natural illumination conditions. Their experiments however achieved only 0.01% of the theoretically estimated current, showing that much optimization is necessary to achieve practical ferroelectric nematic-based mechano-electric transduction.

The piezoelectric effects observed experimentally so far in liquid crystals and liquid crystal elastomers with their typical values at the given frequencies are summarized in Table 7.

IV. Challenges and outlook

A piezoelectric response is strongly linked to the symmetry axes of the material. These axes can be difficult to control for soft materials such as the ferroelectric nematic liquids. For example, to determine the individual coupling constants, a ferroelectric nematic specimen is required with known, controllable and homogenous polarization. As Fig. 9 shows, the measurement of $\gamma_{3,33}$ in a thin-film sample requires uniform homeotropic alignment, but the internal depolarization field frustrates this alignment. Planar alignment, that is required to measure the other two piezoelectric constants, is more straightforward to achieve with an appropriate surface alignment layer. However, even with a uniform polarization field at

Table 7 Piezoelectric effects observed experimentally in liquid crystals and liquid crystal elastomers, with their typical values at given frequencies

LC phase	Measured coupling constant in pC N^{-1}@frequency in kHz	Characteristics
SmA* (phospholipids)	100 at 0.08[38]	Director tilt induces polarization normal to the bilayers in cell membranes
SmC*	Elastomer: 30@<0.1; 2D fluid: $\gamma_{1,23} \sim 5000@<1$; $\gamma_{3,33} \sim 3000@0.5$[42]	γ_{123}: related to rotation of the director on tilt cone; γ_{333}: due to tilt angle variation
Col_t^*	1@<5[40]	
SmC_sP_F	$\gamma_{3,33} \approx 2\gamma_{3,22} \approx 100$ nC N^{-1}.[200]	Converse piezoelectric effect of a bent-core synclinic ferroelectric liquid crystal
N_F	$\gamma_{3,33} \sim 1000@<6$;[64] $\gamma_{1,13} \sim 3000@<1$ [this paper]	Converse piezoelectric responses of ferroelectric nematic liquid crystals

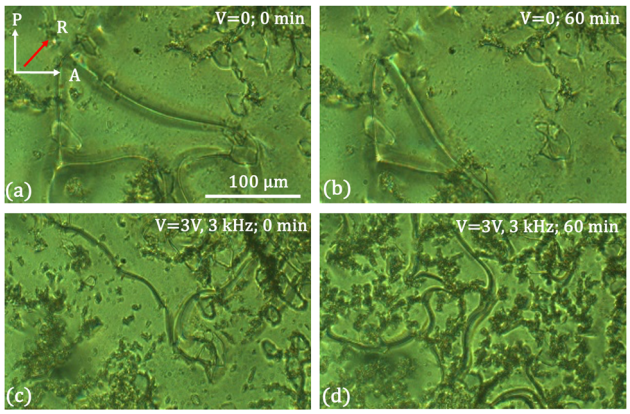

Fig. 12 Textures of a 50 μm KPA-02 sample under zero electric field (a) and (b) and under 3 V, 3 kHz voltage applied (c) and (d) at 0 min (a) and (c) and 60 min (b) and (d) after alignment (a) and (b) and after the field is applied (c) and (d).

the outset, there is always the possibility of material flow, resulting in non-uniform alignment. In fact, for relatively thick N_F films, there are always defects that anneal only slowly thus leading to a varying alignment even at zero electric field applied. An example is shown in Fig. 12 for a 50 μm KPA-02 sample under a zero electric field (Fig. 12(a and b)) and under 3 V, 3 kHz voltage applied (Fig. 12(c and d)) at 0 min (Fig. 12(a and c)) and 60 min (Fig. 12(b and d)) after alignment (Fig. 12(a and b)) and after field applied (Fig. 12(c and d)).

It can be seen that the defects eventually shrink when no field is applied, while new defects are generated after as low as 3 V/50 μm field is applied at 3 kHz. These observations agree with recent papers that showed that DC or AC voltages can induce realignment and formation of various patterns without any threshold.[209–211]

A similar problem can occur during the investigation of the direct piezoelectric effect, where the sample is deformed. The deformation can induce flow in the sample which is also coupled to the orientation of the director field *via* the flow alignment.[212] To decrease the reorientation effect of the electric field or the flow, the applied voltage and the deformation should be small enough to minimize the effect of these phenomena.

An additional complication arises because of the mobility of any ionic species (and it is not possible to make ion-free preparations), which is many orders of magnitude larger in fluids than in crystalline solids. Because of this, ionic motion and the resulting screening of electric fields are factors that always must be considered; this of course is of particular importance at a lower frequency.

Another unexpected parameter that appears to affect the measured piezoelectric coupling constant is the thickness of the ferroelectric nematic film. This is illustrated in Fig. 13a, where the amplitude of the converse piezoelectric vibration is shown for the prototypical ferroelectric nematic liquid crystal, RM734[54] as a function of applied voltage at T = 120 °C under f = 4 kHz signal (Fig. 13(a)) for different film thicknesses between 100 μm and 540 μm. The samples with $d > 300$ μm thicknesses were filled with the liquid crystal at 300 μm film thickness and then the separation between plates was increased. This means that at $d \leq 300$ μm we have films that fill the whole area, while at $d > 300$ μm we have a bridge that does not fill the entire area (see the inset in Fig. 13(a)).

It can be seen that below 3 V, the voltage dependences are linear for all film thicknesses, but the slope of the curves, *i.e.*, the value of the piezoelectric constant ($\gamma = A_f/V$), strongly increases with the film thickness. Above 3 V, the voltage dependence is not linear anymore, which is probably due to the field-induced director realignment that leads to the generation of quadratic (electrostriction effect) and other higher harmonics. The study of the higher harmonic signals can also be done by the lock-in technique by simply choosing *nf* modes with n = 2, 3,.... This should also be one of the tasks of future studies.

In Fig. 13(b), we show the temperature dependence of the converse piezoelectric signal for a film of thickness d = 450 μm of RM734. As already shown by Máthé *et al.*,[64] the piezoelectric signal vanishes in the conventional nematic phase as N has an inversion symmetry. In the N_F phase, it increases roughly proportionally to the value of the ferroelectric polarization measured by Chen *et al.*,[60] indicating no significant realignment on cooling. However, the values for heating are slightly different from those measured for cooling, indicating some alignment effects.

We also note that there is a narrow range at the top of the N_F phase with a slight increase in the effective piezoelectric constant. This range coincides with a modulated phase (N_X) range, as shown recently by Thoen *et al.*;[213] however, it is not clear why that produces an increased piezoelectric response.

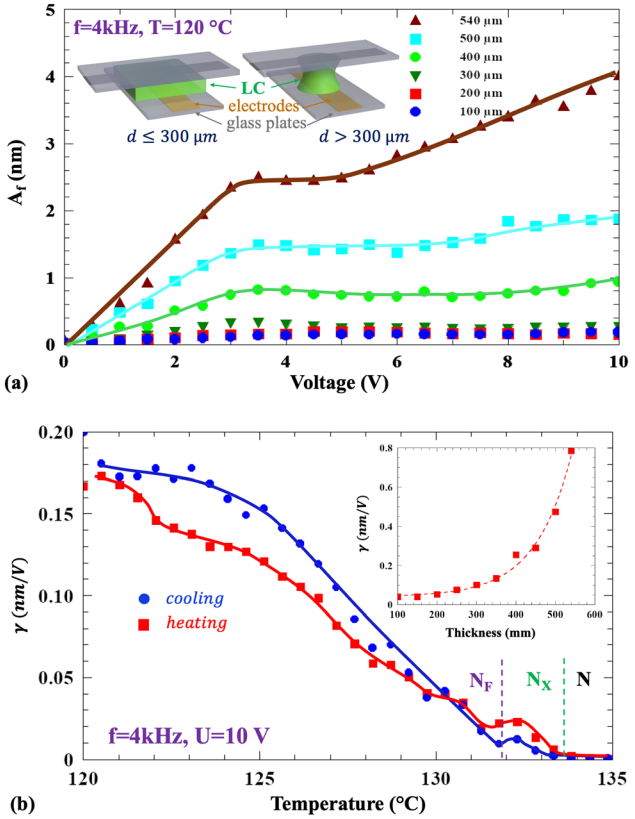

Fig. 13 Measurement of the electric field-induced vibration amplitude A_f of the cover glass normal to the film at a frequency of 4 kHz applied between the substrates of non-oriented RM734 films. (a) Voltage dependence at 120 °C between 0 and 10 V for films with thicknesses between 0.1 mm and 0.54 mm. The inset shows the LC cell geometries for $d \leq 300$ μm and $d > 300$ μm thicknesses. (b) Temperature dependence of the vibration amplitude A_f under $U = 10$ V, $f = 4$ kHz applied voltage measured in a $d = 400$ μm-thick film in heating (red) and cooling (blue) at a rate of 1 °C min^{-1}. The inset shows the film thickness dependence of the effective piezoelectric coupling constant.

That observation indicates the need for the study of the effect in SmZ_A[214,215] and the other modulated, such as the splayed (N_S)[59] phase.

The film thickness dependence of the piezoelectric constant is shown in the inset of Fig. 13(b). The piezoelectric constant is almost constant below about 200 μm thickness and then increases exponentially. What can be the reason for this anomalous thickness dependence? One can think about the effect of surface tension (σ) that leads to a pressure $p = 2\sigma/R$, where $R = \frac{d}{2\sin(\alpha)}$ is the curvature radius, d is the film and α is the contact angle between the glass and the liquid crystal. With typical surface tension values of $\sigma \sim 0.03$ N m^{-1} and $\alpha < 90°$, we get $p < \frac{0.12}{d}$Pa. For $d \sim 100$ μm, this means $p \sim 10^3$ Pa, which is much smaller than of the effective modulus $G = 2\pi\eta \cdot f$, which at $\eta \sim 1$ Pa s is $G \sim 2.4 \times 10^5$ Pa. This means that we do not expect significant effect of the surface tension. Another more likely possibility is an effective increase in the angle of the effective polarization with respect to the film surface at increasing film thickness. By increasing the gap between the glass plates, the morphology of the liquid changes significantly as the inset of Fig. 13(a) illustrates for gap sizes that are smaller or close to the gap where the sample was filled and for gaps that are bigger, respectively. The reason for this film thickness dependence of the polarization direction is not clear and it will be one of the tasks of future work.

Finally, we note the need for quantitative and systematic studies of the direct piezoelectric signals in the fluid N_F phase.

Conflicts of interest

There are no conflicts to declare.

Data availability

Data are available from the corresponding authors upon reasonable request.

Acknowledgements

This work was financially supported by the US National Science Foundation under grant DMR-2210083 and the Hungarian National Research, Development, and Innovation Office under grants NKFIH FK142643, 2023-1.2.1-ERA_NET-2023-00008. P. S. was supported by the János Bolyai Research Scholarship of the Hungarian Academy of Sciences (HAS).

References

1 J. Curie and P. Curie, *Comptes rendus*, 1880, **91**, 294.
2 M. G. Lippmann, *J. Phys. Theor. Appl.*, 1881, 381–394.
3 M. G. Lippmann, *C. R. Acad. Bulg. Sci.*, 1881, **92**, 1049.
4 J. Curie and P. Curie, *C. R. Acad. Bulg. Sci.*, 1884, **93**, 1137.
5 W. P. Mason, *J. Acoust. Soc. Am.*, 1981, **70**, 1561–1566.
6 W. Voigt, *Abh. Gott.*, 1894, **36**, 1.
7 J. Lewiner, *Jpn. J. Appl. Phys.*, 1991, **30**, 5.
8 P. Langevin, *French Pat.*, 505703, 1918.
9 W. G. Cady, *Proc. Inst. Radio Eng.*, 1922, **10**, 83–114.
10 W. G. Cady, *Piezoelectricity: An introduction to the Theory and Applications of Electromechanical Phenomena in Crystals*, McGraw-Hill Book Company Inc., New York, 1946.
11 S. Roberts, *Phys. Rev.*, 1947, **71**, 890–895.
12 A. Von Hippel, R. G. Breckenridge, F. G. Chesley and L. Tisza, *Ind. Eng. Chem.*, 1946, **38**, 1097–1109.
13 B. M. Wul and I. M. Goldman, *Akad. Nauk.*, 1945, **49**, 179–182.
14 E. Fukada, *Ultrasonics*, 1968, 229–234.
15 Y. Wada and R. Hayakawa, *Jpn. J. Appl. Phys.*, 1976, **15**, 2041–2057.
16 J. Jacob, N. More, K. Kalia and G. Kapusetti, *Inflamm. Regen.*, 2018, **38**, 2.
17 N. A. Kamel, *Biophys. Rev.*, 2022, **14**, 717–733.
18 C. A. L. Bassett, *Calcif. Tissue Res.*, 1967, **1**, 252–272.

19 H. Kawai, *Jpn. J. Appl. Phys.*, 1969, **8**, 975.
20 H. Kawai, *Jpn. J. Appl. Phys.*, 1969, **8**, 975.
21 J. Lekkala, R. Poramo, K. Nyholm and T. Kaikkonen, *Med. Biol. Eng. Comput.*, 1996, **34**, 67–68.
22 G. M. Sessler and J. Hillenbrand, *Appl. Phys. Lett.*, 1999, **75**, 3405.
23 X. Zhang, G. M. Sessler and J. Hillenbrand, *J. Electrostat.*, 2007, **65**, 94–100.
24 S. Bauer, R. Gerhard-Multhaupt and G. M. Sessler, *Phys. Today*, 2004, **57**, 37.
25 J. Morvan, E. Buyuktanir, J. L. West and A. Jákli, *Appl. Phys. Lett.*, 2012, **100**, 063901.
26 M. Varga, J. Morvan, N. Diorio, E. Buyuktanir, J. Harden, J. L. West and A. Jákli, *Appl. Phys. Lett.*, 2013, **102**, 153903.
27 N. Sezer and M. Koç, *Nano Energy*, 2021, **80**, 105567.
28 J. F. Tressler, S. Alkoy and R. E. Newnham, *J. Electroceram.*, 1998, **2**, 257–272.
29 Z. L. Wang and W. Wu, *MRS Bull.*, 2025, **50**, 115–122.
30 P. Curie, *J. Phys. Theor. Appl.*, 1894, 393–415.
31 J. F. Nye, *Physical Properties of Crystals Their Representation by Tensors and Matrices*, Clarendon Press, 2nd edn, 1985.
32 R. Carter and R. Kensley, *Introduction-to-Piezoelectric-Transducers*, 2022.
33 J.-F. Li, *Lead-Free Piezoelectric Materials*, Wiley-VCH, Beijing, 2021, pp. 1–18.
34 M. I. Hossain and G. J. Blanchard, *J. Phys. Chem. Lett.*, 2023, **14**, 2731–2735.
35 M. I. Hossain, H. Wang, L. Adhikari, G. A. Baker, A. Mezzetta, L. Guazzelli, P. Mussini, W. Xie and G. J. Blanchard, *J. Phys. Chem. B*, 2024, **128**, 1495–1505.
36 N. Sebastián, M. Čopič and A. Mertelj, *Phys. Rev. E*, 2022, **106**, 021001.
37 A. Jakli, *J. Appl. Phys.*, 1999, **85**, 1101–1104.
38 A. Jákli, *Liq. Cryst.*, 2010, **37**, 825–837.
39 A. Jákli, N. Éber, L. Bata, A. Jakli and N. Eber, *Polym. Adv. Technol.*, 1992, **3**, 269–274.
40 A. Jákli, M. Muller, D. Kruerke, G. Heppke and A. Jakli, *Liq. Cryst.*, 1998, **24**, 467–472.
41 A. Jákli and A. Saupe, *One- and Two-Dimensional Fluids: Properties of Smectic, Lamellar and Columnar Liquid Crystals*, Taylor and Francis, Boca Raton, 1st edn, 2006.
42 A. Jakli and A. Saupe, *Mol. Cryst. Liq. Cryst.*, 1993, **237**, 389–398.
43 A. Jákli and N. Éber, in *Handbook of Liquid Crystals*, ed. J. W. Goodby, P. J. Collings, T. Kato, C. Tschierske, H. F. Gleeson and P. Raynes, Wiley-VCH, Weinheim, 2nd edn, 2014, pp. 751–772.
44 A. Jákli and N. Éber, *Modern Topics in Liquid Crystals: From Neutron Scattering to Ferroelectricity*, 1993, p. 235.
45 A. Jákli and A. Saupe, *Liq. Cryst.*, 1991, **9**, 519–526.
46 A. I. Jakli and A. Saupe, *Mol. Cryst. Liq. Cryst.*, 1997, **292**, 293–300.
47 A. Jákli, J. Harden, C. Notz and C. Bailey, *Liq. Cryst.*, 2008, **35**, 395–400.
48 A. Jakli, L. Bata, A. Buka and N. Eber, *Ferroelectrics*, 1986, **69**, 153–163.
49 A. Jakli, L. Bata, A. Buka and I. Janossy, *J. Physique Lett.*, 1985, **46**, L759–L761.
50 R. B. Meyer, *Mol. Cryst. Liq. Cryst.*, 1977, **40**, 33–48.
51 R. B. Meyer, L. Liebert, L. Strzelecki and P. Keller, *J. Phys., Lett.*, 1975, **36**, 69–71.
52 H. Bock and W. Helfrich, *Liq. Cryst.*, 1992, **12**, 697–703.
53 T. Niori, T. Sekine, J. Watanabe, T. Furukawa and H. Takezoe, *J. Mater. Chem.*, 1996, **6**, 1231–1233.
54 R. J. Mandle, S. J. Cowling and J. W. Goodby, *Phys. Chem. Chem. Phys.*, 2017, **19**, 11429–11435.
55 H. Nishikawa, K. Shiroshita, H. Higuchi, Y. Okumura, Y. Haseba, S. I. Yamamoto, K. Sago and H. Kikuchi, *Adv. Mater.*, 2017, **29**, 1702354.
56 N. Sebastián, M. Čopič and A. Mertelj, *Phys. Rev. E*, 2022, **106**, 021001.
57 R. J. Mandle, N. Sebastián, J. Martinez-Perdiguero and A. Mertelj, *Nat. Commun.*, 2021, **12**, 4962.
58 N. Sebastián, L. Cmok, R. J. Mandle, M. R. De La Fuente, I. Drevenšek Olenik, M. Čopič and A. Mertelj, *Phys. Rev. Lett.*, 2020, **124**, 037801.
59 A. Mertelj, L. Cmok, N. Sebastián, R. J. Mandle, R. R. Parker, A. C. Whitwood, J. W. Goodby and M. Čopič, *Phys. Rev. X*, 2018, **8**, 041025.
60 X. Chen, E. Korblova, D. Dong, X. Wei, R. Shao, L. Radzihovsky, M. A. Glaser, J. E. Maclennan, D. Bedrov, D. M. Walba and N. A. Clark, *Proc. Natl. Acad. Sci. U. S. A.*, 2020, **117**, 14021–14031.
61 M. T. Máthé, H. Nishikawa, F. Araoka, A. Jákli and P. Salamon, *Nat. Commun.*, 2024, **15**, 6928.
62 A. I. Jarosik, H. Nádasi, M. I. Schwidder, A. I. Manabe, M. I. Bremer, M. I. Klasen-Memmer and A. Eremin, *Proc. Natl. Acad. Sci. U. S. A.*, 2024, **121**, e2313629121.
63 M. T. Máthé, K. Perera, A. Buka, P. Salamon and A. Jákli, *Adv. Sci.*, 2024, **11**, 2305950.
64 M. T. Máthé, M. S. H. Himel, A. Adaka, J. T. Gleeson, S. Sprunt, P. Salamon and A. Jákli, *Adv. Funct. Mater.*, 2024, 2314158.
65 P. Medle Rupnik, L. Cmok, N. Sebastián and A. Mertelj, *Adv. Funct. Mater.*, 2024, 2402554.
66 R. Bechmann, *Phys. Rev.*, 1958, **110**, 1060.
67 D. A. Berlincourt, C. Cmolik and H. Jaffe, *Proc. IRE*, 1960, **48**, 220–229.
68 D. Berlincourt and H. H. A. Krueger, *J. Appl. Phys.*, 1959, **30**, 1804–1810.
69 M. J. Lodeiro, M. Stewart and M. G. Cain, in *NPL Report DEPC MPR 040*, Controller of HMSO and Queen's Printer for Scotland, Middlesex, 2005, pp. 1–42.
70 S. Gorfman and N. Zhang, *Piezoelectric Materials: from Fundamentals to Emerging Applications*, 2024, vol. 1–2, pp. 17–32.
71 M. Stewart and M. G. Cain, in *Characterisation of Ferroelectric Bulk Materials and Thin films*, ed. M. G. Cain, Dordrecht Springer, 1st edn, 2014, pp. 37–64.
72 J. Fialka and P. Benes, *IEEE Trans. Instrum. Meas.*, 2013, **62**, 1047–1057.
73 S. Gorfman, O. Schmidt, U. Pietsch, P. Becker and L. Bohatý, *Z. Kristallogr.*, 2007, **222**, 396–401.

74 M. Acharya, D. Lou, A. Fernandez, J. Kim, Z. Tian and L. W. Martin, *Phys. Rev. Appl.*, 2023, **20**, 014017.
75 P.-G. de Gennes, *Phys. Today*, 1974, **5**, 333.
76 V. G. Chigrinov, V. M. Kozenkov and H.-S. Kwok, *Photoalignment of Liquid Crystalline Materials*, Wiley, West Sussex, England, 2008.
77 C. P. McGinty, J. Kołacz and C. M. Spillmann, *Appl. Phys. Lett.*, 2021, **119**, 141111.
78 J. Harden, M. Chambers, R. Verduzco, P. Luchette, J. T. Gleeson, S. N. Sprunt and A. Jákli, *Appl. Phys. Lett.*, 2010, **96**, 102907.
79 J. Hao, W. Li, J. Zhai and H. Chen, *Mater. Sci. Eng., R*, 2019, **135**, 1–57.
80 M. Habib, I. Lantgios and K. Hornbostel, *J. Phys. D: Appl. Phys.*, 2022, **55**, 423002.
81 E. Sawaguchi, *J. Phys. Soc Japan*, 1953, **8**, 615–629.
82 Z. Butt, R. A. Pasha, F. Qayyum, Z. Anjum, N. Ahmad and H. Elahi, *J. Mech. Sci. Technol.*, 2016, **30**, 3553–3558.
83 N. P. Maria Joseph Raj, A. Ks, G. Khandelwal, N. R. Alluri and S. J. Kim, *Sustain. Energy Fuels*, 2020, **4**, 5636–5644.
84 H. He, W. Lu, J. A. S. Oh, Z. Li, X. Lu, K. Zeng and L. Lu, *ACS Appl. Mater. Interfaces*, 2020, **12**, 30548–30556.
85 K. Reichmann, A. Feteira and M. Li, *Materials*, 2015, **8**(12), 8467–8495.
86 C. Groh, D. J. Franzbach, W. Jo, K. G. Webber, J. Kling, L. A. Schmitt, H. J. Kleebe, S. J. Jeong, J. S. Lee and J. Rödel, *Adv. Funct. Mater.*, 2014, **24**, 356–362.
87 E. Hollenstein, M. Davis, D. Damjanovic and N. Setter, *Appl. Phys. Lett.*, 2005, **87**, 1–3.
88 O. Tokay and M. Yazıcı, *Mater. Today Commun.*, 2022, **31**, 103358.
89 Y. Saito, H. Takao, T. Tani, T. Nonoyama, K. Takatori, T. Homma, T. Nagaya and M. Nakamura, *Nature*, 2004, **432**, 84–87.
90 P. Li, Y. Huan, W. Yang, F. Zhu, X. Li, X. Zhang, B. Shen and J. Zhai, *Acta Mater.*, 2019, **165**, 486–495.
91 P. Li, J. Zhai, B. Shen, S. Zhang, X. Li, F. Zhu, X. P. Zhang Li, J. Zhai, B. Shen, S. Zhang, X. Li, F. Zhu and X. Zhang, *Adv. Mater.*, 2018, **30**, 1705171.
92 M. Dunce, B. Garbarz-Glos, I. Smeltere, M. Antonova and M. Livinsh, *Electrical and mechanical properties of KNN based lead-free ceramics*, 2011.
93 O. Tokay and M. Yazıcı, *Mater. Today Commun.*, 2022, **31**, 103358.
94 J. Rödel, W. Jo, K. T. P. Seifert, E. M. Anton, T. Granzow and D. Damjanovic, *J. Am. Ceram. Soc.*, 2009, **92**, 1153–1177.
95 J. Hao, W. Li, J. Zhai and H. Chen, *Mater. Sci. Eng., R*, 2019, **135**, 1–57.
96 I. L. Guy, S. Muensit and E. M. Goldys, *Appl. Phys. Lett.*, 1999, **75**, 4133–4135.
97 R. Hou, D. Hutson and K. J. Kirk, *Insight – Non-Destruct. Test. Cond. Monit.*, 2013, **55**, 302–307.
98 R. Yimnirun, E. Meechoowas, S. Ananta and T. Tunkasiri, *CMU J.*, 2004, **3**, 147–154.
99 W. Liu, Y. Cao, J. Wang, Y. Wang, X. Xi and J. Yang, *Mater. Sci. Eng. B*, 2021, **263**, 114847.
100 R. Zhang, W. Jiang, B. Jiang and W. Cao, *AIP Conf. Proc.*, 2002, **626**, 188–197.
101 B. Bauer, *IRE Trans. Audio*, 1956, **AU-4**, 94–98.
102 A. Safari and K. E. Akdogan, *Piezoelectric and Acoustic Materials for Transducer Applications*, Springer Science + Business Media, LLC, 2010.
103 M. K. Rahman, M. F. Hossain, K. M. Shorowordi and M. A. Matin, *Appl. Mech. Mater.*, 2016, **860**, 129–133.
104 R. Hou, D. Hutson and K. J. Kirk, *Insight - Non-destructive Testing and Condition Monitoring*, 2013, **55**(6), 302–307.
105 A. W. Warner, M. Onoe and G. A. Coquin, *J. Acoust. Soc. Am.*, 1967, **42**, 1223–1231.
106 M. Al Ahmad and R. Plana, *Int. J. Microw. Wirel. Technol.*, 2009, **1**, 5–9.
107 R. Wang, S. A. Bhave and K. Bhattacharjee, *J. Microelectromech. Syst.*, 2015, **24**, 300–308.
108 Y. Yang, R. Lu, T. Manzaneque and S. Gong, in IFCS 2018 – IEEE International Frequency Control Symposium, Institute of Electrical and Electronics Engineers Inc., 2018.
109 V. Plessky, S. Yandrapalli, P. J. Turner, L. G. Villanueva, J. Koskela and R. B. Hammond, *Electron. Lett.*, 2019, **55**, 98–100.
110 R. Agrawal and H. D. Espinosa, *Nano Lett.*, 2011, **11**, 786–790.
111 J. Zhou, P. Fei, Y. Gao, Y. Gu, J. Liu, G. Bao and Z. L. Wang, *Nano Lett.*, 2008, **8**, 2725–2730.
112 Q. He, X. Li, J. Zhang, H. Zhang and J. Briscoe, *Nano Energy*, 2021, **85**, 105938.
113 H. S. Kim, J. H. Kim and J. Kim, *Int. J. Precis. Eng. Manuf.*, 2011, **12**, 1129–1141.
114 Y. Yan, K.-H. Cho, D. Maurya, A. Kumar, S. Kalinin, A. Khachaturyan and S. Priya, *Appl. Phys. Lett.*, 2013, **102**, 042903.
115 F. Li, M. J. Cabral, B. Xu, Z. Cheng, E. C. Dickey, J. M. LeBeau, J. Wang, J. Luo, S. Taylor, W. Hackenberger, L. Bellaiche, Z. Xu, L.-Q. Chen, T. R. Shrout and S. Zhang, *Science*, 2019, **364**, 264–268.
116 S. Xu, Y. W. Yeh, G. Poirier, M. C. McAlpine, R. A. Register and N. Yao, *Nano Lett.*, 2013, **13**, 2393–2398.
117 F. Wu, W. Cai, Y.-W. Yeh, S. Xu and N. Yao, *Sci. Rep.*, 2016, **6**, 22513.
118 Q. Li, Y. Liu, J. Liu, K. Song, H. Guo, F. Li and Z. Xu, *Adv. Funct. Mater.*, 2022, **32**, 2201719.
119 L. Bian, X. Qi, K. Li, Y. Yu, L. Liu, Y. Chang, W. Cao and S. Dong, *Adv. Funct. Mater.*, 2020, **30**, 2001846.
120 K. S. Ramadan, D. Sameoto and S. Evoy, *Smart Mater. Struct.*, 2014, **23**, 033001.
121 K. K. Sappati and S. Bhadra, *Sensors*, 2018, **18**, 3605.
122 N. Soin, T. H. Shah, S. C. Anand, J. Geng, W. Pornwannachai, P. Mandal, D. Reid, S. Sharma, R. L. Hadimani, D. V. Bayramol and E. Siores, *Energy Environ. Sci.*, 2014, **7**, 1670–1679.
123 S. M. Damaraju, S. Wu, M. Jaffe and T. L. Arinzeh, *Biomed. Mater.*, 2013, **8**, 045007.

124 J. Y.-H. Kim, A. Cheng and Y.-C. Tai, in IEEE, 2011, pp. 473–476.
125 Q. Zhu, X. Song, X. Chen, D. Li, X. Tang, J. Chen and Q. Yuan, *Nano Energy*, 2024, **127**, 109741.
126 J. D. Sherman, J. Elloian, J. Jadwiszczak and K. L. Shepard, *ACS Appl. Polym. Mater.*, 2020, **2**, 5110–5120.
127 X. Fan, M. Sun, Z. Li, Z. Chen, X. Zhou, Q. Lu and Z. Zhang, *React. Funct. Polym.*, 2022, **180**, 105391.
128 J. Wu, Y. Fu, G.-H. Hu, S. Wang and C. Xiong, *Polymers*, 2021, **13**, 2037.
129 S. Anwar, M. Hassanpour Amiri, S. Jiang, M. M. Abolhasani, P. R. F. Rocha and K. Asadi, *Adv. Funct. Mater.*, 2021, **31**, 2004326.
130 R. G. Kepler and R. A. Anderson, *Adv. Phys.*, 1992, **41**, 1–57.
131 V. Bhavanasi, V. Kumar, K. Parida, J. Wang and P. S. Lee, *ACS Appl. Mater. Interfaces*, 2016, **8**, 521–529.
132 M. S. Kim, H. R. Ahn, S. Lee, C. Kim and Y. J. Kim, *Sens. Actuators, A*, 2014, **212**, 151–158.
133 C. Li, P. M. Wu, S. Lee, A. Gorton, M. J. Schulz and C. H. Ahn, *J. Microelectromech. Syst.*, 2008, **17**, 334–341.
134 S. Khan, S. Tinku, L. Lorenzelli and R. S. Dahiya, *IEEE Sens. J.*, 2015, **15**, 3146–3155.
135 S. Gupta, F. Giacomozzi, H. Heidari, L. Lorenzelli and R. Dahiya, *Procedia Engineering*, Elsevier Ltd, 2016, vol. 168, pp. 662–665.
136 H. Gong, X. Wang, M. Sun, Y. Zhang, Q. Ji and Z. Zhang, *ACS Omega*, 2022, **7**, 42949–42959.
137 J. Wu, Y. Fu, G.-H. Hu, S. Wang, C. Xiong, H. Kaczmarek and J. Kowalonek, *Polymers*, 2021, **13**, 2037.
138 K. S. Ramadan, D. Sameoto and S. Evoy, *Smart Mater. Struct.*, 2014, **23**, 033001.
139 J. Sun, H. Guo, J. Ribera, C. Wu, K. Tu, M. Binelli, G. Panzarasa, F. W. M. R. Schwarze, Z. L. Wang and I. Burgert, *ACS Nano*, 2020, **14**, 14665–14674.
140 Suprapto, Y. Ting, H. Gunawan, E. Yazid, A. S. Nugraha, B. Azhari, M. L. Ramadiansyah, M. F. Hikmawan and Jubaidah, *Polym. Int.*, 2024, **73**, 727–747.
141 G. Tian, W. Deng, Y. Gao, D. Xiong, C. Yan, X. He, T. Yang, L. Jin, X. Chu, H. Zhang, W. Yan and W. Yang, *Nano Energy*, 2019, **59**, 574–581.
142 B. Zhou, R. Li, J. Cai, J. Xu, Z. Zhao and J. Pei, *Mater. Res. Express*, 2018, **5**, 095510.
143 W. Choi, K. Choi, G. Yang, J. C. Kim and C. Yu, *Polym. Test.*, 2016, **53**, 143–148.
144 S. Siddiqui, D. Il Kim, E. Roh, L. T. Duy, T. Q. Trung, M. T. Nguyen and N. E. Lee, *Nano Energy*, 2016, **30**, 434–442.
145 Y. Yang, H. Pan, G. Xie, Y. Jiang, C. Chen, Y. Su, Y. Wang and H. Tai, *Sens. Actuators, A*, 2020, **301**, 11789.
146 X. Gao, M. Zheng, X. Yan, J. Fu, Y. Hou and M. Zhu, *Nanoscale*, 2020, **12**, 5175–5185.
147 Y. Zhang, C. K. Jeong, J. Wang, H. Sun, F. Li, G. Zhang, L. Q. Chen, S. Zhang, W. Chen and Q. Wang, *Nano Energy*, 2018, **50**, 35–42.
148 S. Bauer, R. Gerhard-Multhaupt and G. M. Sessler, *Phys. Today*, 2004, **57**, 37–43.
149 O. Hamdi, F. Mighri and D. Rodrigue, *AIMS Mater. Sci.*, 2018, **5**, 845–869.
150 A. Mohebbi, F. Mighri, A. Ajji and D. Rodrigue, *Adv. Polym. Technol.*, 2018, **37**, 468–483.
151 G. Buchberger, R. Schwödiauer and S. Bauer, *Appl. Phys. Lett.*, 2008, **92**, 123511.
152 Y. Cao, W. Li and N. Sepulveda, *IEEE Sens. J.*, 2019, **19**, 10327–10335.
153 C. Song, J. Zhao, X. Ma, M. Zhang, W. Yuan, F. Yang, Z. Wang, X. Zhang and Y. Pan, *AIP Adv.*, 2021, **11**, 115002.
154 P. Fang, X. Ma, X. Li, X. Qiu, R. Gerhard, X. Zhang and G. Li, *IEEE Sens. J.*, 2018, **18**, 401–412.
155 J. Hillenbrand, M. Kodejska, Y. Garcin, H. Von Seggern and G. M. Sessler, *IEEE Trans. Dielectr. Electr. Insul.*, 2010, **17**, 1021–1027.
156 Q. Zhuo, L. Tian, P. Fang, G. Li and X. Zhang, in 5th Annual IEEE International Conference on Cyber Technology in Automation, Control and Intelligent Systems, Shenyang, 2015, pp. 918–921.
157 F. Owusu, F. A. Nüesch and D. M. Opris, *Adv. Funct. Mater.*, 2022, **32**, 2207083.
158 J. Wen, W. Wu, Z. Xie and J. Wu, *Macromol. Mater. Eng.*, 2023, **308**, 2300101.
159 F. Owusu, F. A. Nüesch and D. M. Opris, *Adv. Funct. Mater.*, 2022, **32**, 2207083.
160 M. Varga, J. Morvan, N. Diorio, E. Buyuktanir, J. Harden, J. L. West, A. Jakli and A. Jakli, *Appl. Phys. Lett.*, 2013, **102**, 1–5.
161 J. Morvan, E. Buyuktanir, J. L. West and A. Jákli, *Appl. Phys. Lett.*, 2012, **100**, 063901.
162 E. Fukada, *Ferroelectrics*, 1984, **60**, 285–296.
163 E. Fukada and I. Yasuda, *Jpn. J. Appl. Phys.*, 1964, **3**, 117–121.
164 E. Fukada and I. Yasuda, *Jpn. J. Appl. Phys.*, 1964, **3**, 117.
165 A. A. Marino, R. O. Becker and S. C. Soderholm, *Calcif. Tissue Res.*, 1971, **8**, 177–180.
166 D. Denning, M. T. Abu-Rub, D. I. Zeugolis, S. Habelitz, A. Pandit, A. Fertala and B. J. Rodriguez, *Acta Biomater.*, 2012, **8**, 3073–3079.
167 M. Minary-Jolandan and M.-F. Yu, *Nanotechnology*, 2009, **20**, 085706.
168 D. Denning, M. V. Paukshto, S. Habelitz and B. J. Rodriguez, *J. Biomed. Mater. Res., Part B*, 2014, **102**, 284–292.
169 S. Guerin, A. Stapleton, D. Chovan, R. Mouras, M. Gleeson, C. McKeown, M. R. Noor, C. Silien, F. M. F. Rhen, A. L. Kholkin, N. Liu, T. Soulimane, S. A. M. Tofail and D. Thompson, *Nat. Mater.*, 2018, **17**, 180–186.
170 Y. Song, T. Wu, J. Bao, M. Xu, Q. Yang, L. Zhu, Z. Shi, G. H. Hu and C. Xiong, *Carbohydr. Polym.*, 2022, **288**, 119407.
171 B. Y. Lee, J. Zhang, C. Zueger, W. J. Chung, S. Y. Yoo, E. Wang, J. Meyer, R. Ramesh and S. W. Lee, *Nat. Nanotechnol.*, 2012, **7**, 351–356.
172 Y. Ando and E. Fukada, *J. Polym. Sci., Polym. Phys. Ed.*, 1976, **14**, 63–79.
173 E. Fukada and I. Yasuda, *J. Phys. Soc. Japan*, 1957, **12**, 1158–1162.

174 A. Jákli, J. Harden, C. Notz and C. Bailey, *Liq. Cryst.*, 2008, **35**, 395–400.
175 R. B. Meyer, *Phys. Rev. Lett.*, 1969, **22**, 918–921.
176 J. Harden, N. Diorio, A. G. Petrov and A. I. Jakli, *Phys. Rev. E:Stat., Nonlinear, Soft Matter Phys.*, 2009, **79**, 1–5.
177 R. Wiltschko and W. Wiltschko, *BioEssays*, 2006, **28**, 157–168.
178 R. Wiltschko and W. Wiltschko, *J. Comp. Physiol., A*, 2005, **191**, 675–693.
179 R. B. Meyer and S. Garoff, *Phys. Rev. Lett.*, 1977, **38**, 848–851.
180 C. M. Spillmann, B. R. Ratna and J. Naciri, *Appl. Phys. Lett.*, 2007, **90**, 21911.
181 L. D. Landau and E. M. Lifshitz, *Electrodynamics of Continuous Media – Volume 8 of Theoretical Physics*, Pergamon Press, Oxford, 2nd edn, 1984.
182 X. Chen, V. Martinez, P. Nacke, E. Korblova, A. Manabe, M. Klasen-Memmer, G. Freychet, M. Zhernenkov, M. A. Glaser, L. Radzihovsky, J. E. Maclennan, D. M. Walba, M. Bremer, F. Giesselmann and N. A. Clark, *Proc. Natl. Acad. Sci. U. S. A.*, 2022, **119**, e2210062119.
183 H. Kikuchi, H. Matsukizono, K. Iwamatsu, S. Endo, S. Anan and Y. Okumura, *Adv. Sci.*, 2022, **9**, 2202048.
184 D. M. Walba, E. Körblova, R. Shao, J. E. Maclennan, D. R. Link, M. A. Glaser, N. A. Clark and E. Korblova, *Science*, 2000, **288**, 2181–2184.
185 E. Korblova, E. Guzman, J. Maclennan, M. Glaser, R. Shao, E. Garcia, Y. Shen, R. Visvanathan, N. Clark and D. Walba, *Materials*, 2017, **10**, 1284.
186 D. R. Link, G. Natale, R. Shao, J. E. Maclennan, N. A. Clark, E. Körblova and D. M. Walba, *Science*, 1997, **278**, 1924–1927.
187 A. Jákli, D. Krüerke, H. Sawade and G. Heppke, *Phys. Rev. Lett.*, 2001, **86**, 5715–5718.
188 N. Chattham, E. Korblova, R. Shao, D. M. Walba, J. E. Maclennan and N. A. Clark, *Liq. Cryst.*, 2009, **36**, 1309–1317.
189 P. Pieranski, E. Guyon and P. Keller, *J. Phys.*, 1975, **36**, 1005.
190 A. Jákli and L. Bata, *Mol. Cryst. Liq. Cryst.*, 1991, **201**, 115–124.
191 J. M. Adams and M. Warner, *Phys. Rev. E:Stat., Nonlinear, Soft Matter Phys.*, 2009, **79**, 061704.
192 A. G. Petrov, *The lyotropic state of matter*, Gordon and Breach, 1st edn, 1999.
193 F. Brochard, *Mol. Cryst. Liq. Cryst.*, 1973, **23**, 51–58.
194 F. Kremer, S. U. Vallerien and E. W. Fischer, *Liq Cryst.*, 1991, **9**, 145–150.
195 S. Uto, E. Tazoh, M. Ozaki and K. Yoshino, *J. Appl. Phys.*, 1997, **82**, 2791–2794.
196 S. V. Yablonskii, T. Oue, H. Nambu, A. S. Mikhailov, M. Ozaki and K. Yoshino, *Appl. Phys. Lett.*, 1999, **75**, 64–66.
197 S. Uto, M. Ozaki and K. Yoshino, *Appl. Phys. Lett.*, 1999, **74**, 117–119.
198 A. Jákli, T. Tóth-Katona, T. Scharf, M. Schadt and A. Saupe, *Phys. Rev. E: Stat., Nonlinear, Soft Matter Phys.*, 2002, **66**, 011701.
199 S. U. Vallerien, F. Kremer, E. W. Fischer, H. Kapitza, R. Zentel and H. Poths, *Macromol. Chem. Rapid Commun.*, 1990, **11**, 593–598.
200 A. Jákli, I. C. Pintre, J. L. Serrano, M. B. Ros, M. R. de la Fuente and L. Serrano, *Adv. Mater.*, 2009, **21**, 3784–3788.
201 H. Bock, PhD Thesis, Free University of Berlin, 1994.
202 W. Meier and H. Finkelmann, *Macromolecules*, 1993, **26**, 1811–1817.
203 C.-C. Chang, L.-C. Chien and R. B. Meyer, *Phys. Rev. E: Stat. Phys., Plasmas, Fluids, Relat. Interdiscip. Top.*, 1997, **55**, 534–537.
204 X. Chen, E. Korblova, D. Dong, X. Wei, R. Shao, L. Radzihovsky, M. A. Glaser, J. E. MacLennan, D. Bedrov, D. M. Walba and N. A. Clark, *Proc. Natl. Acad. Sci. U. S. A.*, 2020, **117**, 14021–14031.
205 N. Éber, P. Salamon and Á. Buka, *Liq. Cryst. Rev.*, 2016, **4**, 101–134.
206 M. S. H. Himel, K. Perera, A. Adaka, P. Guragain, R. J. Twieg, S. Sprunt, J. T. Gleeson and A. Jákli, *Adv. Funct. Mater.*, 2024, 2413674.
207 B. Basnet, M. Rajabi, H. Wang, P. Kumari, K. Thapa, S. Paul, M. O. Lavrentovich and O. D. Lavrentovich, *Nat. Commun.*, 2022, **13**, 3932.
208 H. Kamifuji, K. Nakajima, Y. Tsukamoto, M. Ozaki and H. Kikuchi, *Appl. Phys. Express*, 2023, **16**(7), 071003.
209 M. T. Máthé, N. Éber, Á. Buka, H. Nishikawa, F. Araoka, A. Jákli and P. Salamon, *J. Mol. Liq.*, 2025, **428**, 127525.
210 B. Basnet, S. Paladugu, O. Kurochkin, O. Buluy, N. Aryasova, V. G. Nazarenko, S. V. Shiyanovskii and O. D. Lavrentovich, *Nat. Commun.*, 2025, **16**, 1444.
211 K. S. Krishnamurthy, S. K. Prasad, D. S. Shankar Rao, R. J. Mandle, C. J. Gibb, J. Hobbs and N. V. Madhusudana, *Phys. Rev. E*, 2025, **111**, 045420.
212 H. Nishikawa, P. Salamon, M. T. Máthé, A. Jákli and F. Araoka, *Giant*, 2025, **22**, 100356.
213 J. Thoen, G. Cordoyiannis, E. Korblova, D. M. Walba, N. A. Clark, W. Jiang, G. H. Mehl and C. Glorieux, *Phys. Rev. E*, 2024, **110**, 014703.
214 P. Nacke, A. Manabe, M. Klasen-Memmer, X. Chen, V. Martinez, G. Freychet, M. Zhernenkov, J. E. Maclennan, N. A. Clark, M. Bremer and F. Giesselmann, *Sci. Rep.*, 2014, **14**, 4473.
215 N. A. Clark, in 18th International Conference on Ferroelectric Liquid Crystals: Polarity and Chirality in Soft Matter, 2021, vol. 1, p. Pl-2.

